



ELSEVIER

Contents lists available at [ScienceDirect](https://www.sciencedirect.com)

International Journal of Plasticity

journal homepage: www.elsevier.com/locate/ijplas

Numerical study of deformation behavior of rolled AZ31B plate under cyclic loading in different material orientations based on the EVPSC-TDT model

F.H. Wang^a, H. Qiao^{b,*}, Y.Q. Wang^c, J. Dong^a, Y.Y. Jiang^c, P.D. Wu^b

^a National Engineering Research Center of Light Alloy Net Forming & State Key Laboratory of Metal Matrix Composites, Shanghai Jiao Tong University, Shanghai 200240, China

^b Department of Mechanical Engineering, McMaster University, Hamilton, Ontario L8S 4L7, Canada

^c Department of Mechanical Engineering, University of Nevada, Reno NV 89557, United States

ARTICLE INFO

Keywords:

Twinning
Detwinning
Retwinning
Residual twin
Cyclic loading

ABSTRACT

The EVPSC-TDT model is employed to mimic the stabilized stress-strain hysteresis loops of the rolled AZ31B plate under cyclic loading in different material orientations. The predicted stabilized stress-strain hysteresis loops for different material orientations are generally in good agreement with the corresponding experimental data. The key features associated with twinning and detwinning are interpreted in terms of activities of deformation modes. To appropriately mimic the cyclic plastic response of the rolled AZ31B plate, cyclic loading experiments should also be accounted for in determining the Voce-type hardening law parameters in the current model. The equation proposed in the literature is used in the current model to describe the evolution of residual twinning during cyclic loading, and a threshold equation with a new parameter is proposed to constrain fresh twinning and retwinning. The effects of parameters in the two equations on cyclic plastic response are investigated. To approximately describe the apparent easier reverse motion of twin boundaries, the initial CRSS of detwinning is set to be half of that of twinning, and for simplicity the other Voce-type hardening law parameters are kept the same for both twinning and detwinning. The effect of initial CRSS of detwinning on plastic response during reverse loading is also investigated. The inelastic behavior is predicted to occur at the very end of the unloading process for the 90° (ND) material orientation, which is ascribed to detwinning. It is assumed that the magnitude of internal tensile stress upon unloading together with that of the activation stress for detwinning determine when or whether detwinning will occur during unloading. The discrepancies between numerical simulations and experiments of the pseudo-elasticity behavior might be because the current mean field model based on self-consistent schemes might not properly describe some microstructure related properties of the AZ31B plate and so underestimates the internal tensile stresses of twinned grains before unloading, which deserves further investigation.

* Corresponding author at: Department of Mechanical Engineering, McMaster University, Hamilton, Ontario L8S 4L7, Canada.
E-mail address: qiaoh3@mcmaster.ca (H. Qiao).

<https://doi.org/10.1016/j.ijplas.2021.103109>

Received 31 May 2021; Received in revised form 28 August 2021;

Available online 11 September 2021

0749-6419/© 2021 Elsevier Ltd. All rights reserved.

1. Introduction

Magnesium alloys have gained much attention in the past decades for their great potential of applications in the automotive, aircraft, aerospace and transportation industries due to the low density and high specific strength as well as ample global supply of primary magnesium (Nový et al., 2009). Wrought magnesium alloys have superior mechanical properties compared with cast alloys and so have great potential for use as structural components, however, the use of wrought magnesium alloys is very few compared with cast alloys due to the low formability at room temperature of such alloys (Nascimento et al., 2010; You et al., 2017). Wrought Mg alloys suffer from an increased asymmetry of yield behavior and differential work hardening because of the strong texture generated by fabrication process (e.g., rolling or extrusion) (Bettles and Gibson, 2005). The deformation mechanism with strong anisotropy of wrought Mg alloys arises from the limited deformation modes at room temperature and so is closely related to tensile twinning which is the only deformation mode that can provide straining along the c-axis at room temperature. Tensile twinning and detwinning is often observed to alternate during cyclic loading and so play an important role in dictating cycle fatigue behavior of wrought magnesium alloys (Wu et al., 2008).

Extensive experimental studies have been conducted in investigation of the cyclic deformation mechanisms and fatigue of Mg (Yu et al., 2011; Morrow et al., 2014; Murphy-Leonard et al., 2019) or wrought Mg alloys under fully reversed cyclic loading (e.g., Wu et al., 2008; Park et al., 2010; Yu et al., 2012; Hama et al., 2012; Xiong et al., 2012; Wu et al., 2014; Dong et al., 2015; Roostaei and Jahed, 2016; Wang et al., 2019, 2020a, 2020e; Anten and Scholtes, 2019; Ling et al., 2019; Shafaghi et al., 2020; Xie et al., 2021). Efforts have also been made to study the ratcheting behavior and fatigue characteristics of Mg alloys under asymmetric stress-controlled cyclic loading (e.g., Lin et al., 2011; Zhang et al., 2011; Kang et al., 2014; Chen et al., 2015; Castro and Jiang, 2017; Wu et al., 2020; Lei et al., 2021). In addition, studies on the pseudoelastic behavior of Mg alloys under cyclic loading-unloading conditions can also be found in literature (e.g., Cáceres et al., 2003; Mann et al., 2007; Zhou et al., 2008; Muránsky et al., 2009; Lee et al., 2013; Chen et al., 2017; Fallahi et al., 2020; Wang et al., 2020b, J. 2021).

Numerical modeling has been a very powerful tool to assist understanding of deformation mechanisms of HCP metals and becomes very active in very recent years in investigating the twinning and/or detwinning behavior of HCP metals (e.g., Bhattacharyya et al., 2019; Bong et al., 2020; Feng et al., 2020; Feather et al., 2021; Frydrych et al., 2021; Ganesan et al., 2021; Habib et al., 2019; Han et al., 2020; Hu et al., 2021; Indurkar et al., 2020; Lftikhar et al., 2021; Li et al., 2020a, 2020b; Ma et al., 2019; Nakata et al., 2019; Nagra et al., 2020; Paramatmuni et al., 2020, C. 2021; Sahoo et al., 2020; Tang et al., 2020; Wang et al., 2020c, 2020d; Xing et al., 2021; Zhu et al., 2021), however, comparatively scarce numerical studies focusing on study of the cyclic deformation mechanisms of Mg or Mg alloys have been reported in literature. The most common numerical strategies could fall into two categories: continuum phenomenological plasticity approach and crystal plasticity approach. The phenomenological constitutive modeling has a great potential for large-scale simulations of structural components under complex loading conditions due to its relatively low computational cost, and much efforts have been devoted in this aspect to study the cyclic deformation behavior of Mg alloys (e.g., Lee et al., 2008; Li et al., 2010; Kim et al., 2013; Nguyen et al., 2013; Muhammad et al., 2015; Roostaei and Jahed, 2018; Denk et al., 2019; Anes et al., 2019; Lee et al., 2020), however this is beyond the scope of this paper.

Crystal plasticity modeling is another important alternative tool for understanding plastic responses of HCP metals under cyclic loading conditions. In this context, the following crystal plasticity-based models are worth to be mentioned. Firstly, a Taylor-Lin elastoviscoplastic polycrystal model (Lin, 1957; Zouhal et al., 1996; Tóth et al., 2000) accounting for twinning and detwinning was first applied by Gu and Tóth (2012) to model low cycle deformation behavior of AZ31 by using a quantitative volume transfer scheme, and the model was then employed by Gu et al. (2014) using a new variant selection criterion based on the minimum elastic energy of the twin to simulate the fatigue behavior of a AZ31 alloy under small strain amplitudes at room temperature. The Taylor-Lin model is questionable for applications at large strains because it does not account for grain shape evolution and any interaction between a grain and the homogeneous equivalent medium. Secondly, to describe the cyclic deformation of the Mg alloys under stress-controlled cyclic loading conditions, Yu et al. (2014) proposed a crystal plasticity based constitutive model where an explicit scale-transition rule considering the inelastic accommodation of grains was adopted to construct the polycrystalline constitutive model from the single crystal level. The model was successfully employed to describe the uniaxial ratchetting of polycrystalline magnesium alloy at room temperature. Thirdly, the crystal plasticity based finite element (CPFE) has been used to study the inelastic behavior under cyclic loading and unloading (Hama et al., 2013, 2018), and the fatigue behavior under cyclic loading (Briffod et al., 2019), the multi-scale mechanisms of twinning-detwinning under compression and reverse tension (Zhang et al., 2019) in rolled AZ31/AZ31B alloys. Very recently, Jalili et al. (2020) proposed a uniaxial 3D full-field CPFE model to simulate the micro-mechanisms of cyclic plastic deformation of an extruded ZK60 alloy. In addition, Singh et al. (2020) studied the twinning-detwinning behavior of E-form Mg alloy sheets during in-plane reverse loading where the authors used the CPFE simulation to explain the experimentally observed detwinning kinetics. It is noting that in these CPFE models mentioned above, the reorientation scheme associated with twinning and detwinning of the material point was based on the predominant twinning reorientation (PTR) scheme (Tomé et al., 1991). In contrast, Yaghoobi et al. (2020) proposed a multiscale CPFE modeling strategy to capture the deformation mechanisms associated with twinning and detwinning of HCP polycrystals where both the untwinned region and all twin variants could coexist at a material point under Taylor-type constraints. It is also worth mentioning that Zhang et al. (2021a) proposed a phenomenological CPFE model to study the cyclic deformation and fatigue behavior of a Mg-RE alloy that accounted for basal, prismatic and pyramidal slips (including the effect of backstress) and twinning/detwinning. Finally, a twinning and detwinning model (TDT) was proposed by Wang et al. (2012, 2013a) to describe detwinning behavior of HCP metals. The TDT model has been implemented into the elastic-viscoplastic self-consistent (EVPSC) model by Wang et al. (2010b) and the EVPSC-TDT model has been employed to simulate the cyclic shear deformation behavior of an AZ31B sheet (Wang et al., 2015), the cyclic deformation behavior of an extruded ZK60A plate (Qiao et al., 2015b), and

the inelastic deformation behavior of Mg alloys under cyclic loading and unloading (Wang et al., 2013b; Lee et al., 2014, 2020b). To ours' knowledge, the EVPSC-TDT model is one of the most powerful tools to describe twinning and detwinning behavior in HCP metals and has been successfully used to simulate the plastic response of HCP metals under various loading conditions (see Qiao et al., 2021 for a summary). Although the EVPSC-TDT model has been used to either study the cyclic deformation behavior of Mg alloys during only the first few cycles of fully reversed cyclic loadings or analyze the pseudoelastic behavior under cyclic loading and unloading, it has not been employed to investigate the effect of material orientation on the stabilized cyclic plastic deformation of Mg alloys under fully reversed cyclic loadings where the accumulation of residual twins during each cycle will affect the plastic response. It is very important to point out that in the research area of numerical simulation of twinning and detwinning in Mg alloys under cyclic loadings, almost all investigations have been restricted to very few cycles, where both the descriptions of the hardening associated with twinning and residual twinning are not critical because the accumulated plastic strain is limited. When the number of cycles is large, however, both the descriptions become important. Yu et al. (2014) proposed an empirical equation to describe the residual twinning and its accumulation in a Mg single crystal during cyclic loading. They addressed the importance of the empirical equation in predicting the cyclic deformation responses, however, their predictions were not in good agreement with the experimental results, which may be caused by the imposed twinning/detwinning model. In fact, there has not been any numerical work that can successfully simulate the entire cyclic loading process when the number of cycles is large.

In this paper, we aim to study, by using the EVPSC-TDT model, the stabilized plastic deformation behavior of a rolled AZ31B plate under fully reversed cyclic loading in five different material orientations, and with three different strain amplitudes. The equation proposed by Yu et al. (2014) is used in the current model to describe the evolution of residual twinning, and a threshold equation with a new parameter is proposed to constrain fresh twinning and retwinning during cyclic loading. In Section 2, the EVPSC-TDT model is briefly introduced. In Section 3, the deformation behavior of the AZ31B alloy plate under monotonic and cyclic loadings in different material orientations is numerically investigated. The effect of material parameters on cyclic plastic response is then interpreted in terms of activities of various deformation modes, twin volume fractions, plastic shear rate, etc. Meaningful discussions regarding detwinning behavior and residual twinning are also included. The conclusions are drawn in Section 4 based on the simulations.

2. EVPSC-TDT model

In the current study, we aim to investigate the stabilized plastic response of a rolled AZ31B alloy under cyclic loading in different material orientations based on the EVPSC-TDT model. As is well known, the twinning and detwinning mechanisms play an important role in accommodating plastic deformation during cyclic loading. Therefore, the basic concept of the twinning and detwinning (TDT) scheme employed in the current model is necessary to be briefly reviewed although one can refer to the work by Wang et al. (2012, 2013a) for more details. In addition, other relevant input parameters for the model are also introduced here.

The plastic deformation rate, d^p , within a crystal can be calculated as the sum of that due to each of the individual slip or twinning systems, α (e.g., Asaro and Needleman, 1985),

$$d^p = \sum_{\alpha} \dot{\gamma}^{\alpha} \mathbf{P}^{\alpha} \quad (1)$$

where \mathbf{P}^{α} is the Schmid tensor on a given crystallographic plane in a given crystallographic direction, corresponding to the shear rate, $\dot{\gamma}^{\alpha}$, of the slip or twinning system α . The relationship between the resolved shear stress, $\tau^{\alpha} = \mathbf{P}^{\alpha} : \boldsymbol{\sigma}$, within the crystal and the resulting shear rate, $\dot{\gamma}^{\alpha}$, can be described by a power-law viscoplastic constitutive rule ($\boldsymbol{\sigma}$ is the Cauchy stress tensor). For slip, the power-law rule is simply written as,

$$\dot{\gamma}^{\alpha} = \dot{\gamma}_0 \left| \tau^{\alpha} / \tau_{cr}^{\alpha} \right|^{\frac{1}{m}} \text{sgn}(\tau^{\alpha}) \quad (2)$$

where $\dot{\gamma}_0$ is a reference shear rate, m is the strain rate sensitivity, 'sgn' denotes the sign function, and τ_{cr}^{α} is the critical resolved shear stress (CRSS). For twinning, treated as pseudo-slip and described using four operations (A, B, C, and D) in the TDT model, the shear rates associated with the four operations can be respectively denoted as $\dot{\gamma}^{\alpha A}$, $\dot{\gamma}^{\alpha B}$, $\dot{\gamma}^{\alpha C}$, and $\dot{\gamma}^{\alpha D}$. For the detailed expressions of these shear rates, one can refer to Wang et al. (2012).

In the EVPSC-TDT model, a newly generated twin is treated as a new grain (child) and the orientation of the child grain is initially related to that of the parent through the crystallographic-twin relationship. It is important to note that there is no special enforcement equilibrium or compatibility between the twin and the parent, rather, the twin and the parent are forced to satisfy equilibrium and compatibility with the homogeneous equivalent medium that surrounds each of them based on self-consistent schemes (Liao et al., 2016). Four operations are defined in the TDT scheme to describe the twinning and detwinning processes (Wang et al., 2012, 2013a). Operations A and B describe twinning process, while operations C and D handle detwinning. The driving forces for operations A and C are from the parent grain and the child grains provide the driving forces for operations B and D. Based on the defined four operations, the net evolution of twin volume fraction (VF) associated with twin system α can be written as,

$$\dot{f}^{\alpha} = f^0 \left(\dot{f}^{\alpha A} + \dot{f}^{\alpha C} \right) + f^{\alpha} \left(\dot{f}^{\alpha B} + \dot{f}^{\alpha D} \right) \quad (3)$$

where f^0 ($f^0 = 1 - \sum_{\alpha} f^{\alpha}$) is the VF of the parent. $\dot{f}^{\alpha A}$, $\dot{f}^{\alpha B}$, $\dot{f}^{\alpha C}$, and $\dot{f}^{\alpha D}$ respectively denote the evolution of twin VF associated with operations A, B, C and D, and can be calculated as ($\dot{\gamma}^{tw}$ is the characteristic twinning shear),

$$f^{\alpha A} = \frac{|\dot{\gamma}^{\alpha A}|}{\dot{\gamma}^{tw}}, f^{\alpha B} = \frac{|\dot{\gamma}^{\alpha B}|}{\dot{\gamma}^{tw}}, f^{\alpha C} = -\frac{|\dot{\gamma}^{\alpha C}|}{\dot{\gamma}^{tw}}, f^{\alpha D} = -\frac{|\dot{\gamma}^{\alpha D}|}{\dot{\gamma}^{tw}} \quad (4)$$

At the beginning of deformation, the VF of twin system α is zero ($f^\alpha = 0$). If twinning occurs with further straining, f^α should increase with decreasing the VF of the parent, f^0 , during which detwinning could not be activated and the twin VF rates for operations C and D should be zero ($\dot{f}^{\alpha C} = \dot{f}^{\alpha D} = 0$). When detwinning happens, f^α decreases with increasing the VF of the parent, where the twin VF rates for operations A and B are zero ($\dot{f}^{\alpha A} = \dot{f}^{\alpha B} = 0$). If the twin variant formed during previous loading process could not completely be detwinned upon load reversal, residual twin forms and it could accumulate at previous twin boundaries during subsequent cyclic twinning-detwinning process (Yu et al., 2011).

In order to include the evolution of residual twinning during cyclic loading in the current model, the evolution equation of residual twin VF with deformation proposed by Yu et al. (2014) will be employed here,

$$f_{res}^\alpha = f_{sat}^\alpha \left(1 - \exp\left(-\frac{f_c^\alpha}{b_{tw}^\alpha}\right) \right) \quad (5)$$

where f_{res}^α is the residual twin VF for twinning system α , f_{sat}^α denotes the saturated residual twin VF, f_c^α is the accumulated twin VF, b_{tw}^α represents the material parameter governing the rate of saturation of residual twins. As an illustration, Fig. 1 presents the residual twin VF versus the accumulated twin VF plot for twinning system α when the saturated residual twin VF is fixed to be $f_{sat}^\alpha = 0.035$ and the material parameter, b_{tw}^α , is set to be 0.25 or 0.5.

In addition, the extended Voce law (Tomé et al., 1984) will be employed in the current model to describe the threshold stress τ_{cr}^α for slip or twinning system α ,

$$\tau_{cr}^\alpha = \tau_0^\alpha + (\tau_1^\alpha + h_1^\alpha \Gamma) \left(1 - \exp\left(-\frac{h_0^\alpha}{\tau_1^\alpha} \Gamma\right) \right) \quad (6)$$

where τ_0^α , h_0^α , h_1^α and $\tau_0^\alpha + \tau_1^\alpha$ are the initial CRSS, the initial hardening rate, the asymptotic hardening rate, and the back-extrapolated CRSS, respectively. Γ is total accumulated shear strain within the grain due to all slip and twinning systems. The evolution of the threshold stress τ_{cr}^α for slip or twinning system α during plastic deformation can be written as,

$$\dot{\tau}_{cr}^\alpha = \frac{d\tau_{cr}^\alpha}{d\Gamma} \sum_{\beta} h^{\alpha\beta} \dot{\gamma}^\beta \quad (7)$$

where $\dot{\gamma}^\beta$ is the shear rate for slip or twinning system β . $h^{\alpha\beta}$ denotes the latent hardening coupling coefficients which are introduced to empirically account for the obstacles on system α associated with system β .

Finally, it is worth mentioning that a threshold twin VF is introduced here to terminate twinning in a grain as it is rarely observed that twinning can occupy the entire grain during deformation,

$$V^{th} = \min\left(1.0, A_1 + A_2 \frac{V^{eff}}{V^{acc}}\right) \quad (8)$$

where V^{acc} and V^{eff} are two statistical variables denoting the weighted VF of the twinned region and VF of twin terminated grains, respectively. A_1 and A_2 are two material constants.

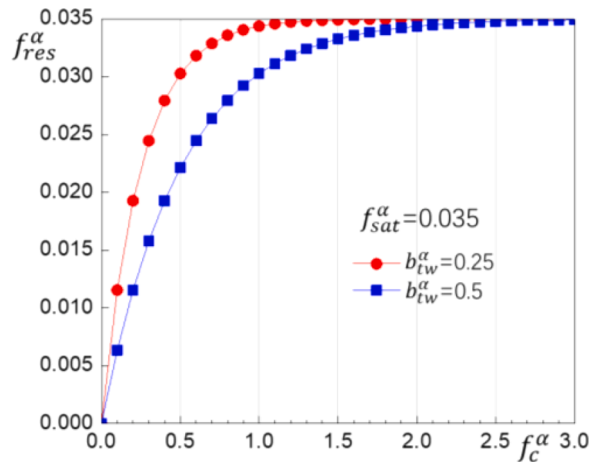


Fig. 1. The residual twin VF versus the accumulated twin VF plot for twinning system α when the saturated residual twin VF is fixed to be $f_{sat}^\alpha = 0.035$ and the material parameter, b_{tw}^α , is set to be 0.25 or 0.5.

3. Results and discussions

The EVPSC-TDT model is employed here to study the stabilized plastic response of a rolled AZ31B plate under cyclic loading in different material orientations. The material studied in the present paper is a rolled AZ31B (Mg-3Al-1Zn-0.5Mn) alloy consisting of mostly equiaxed grains with an average grain size of approximately 50 μm . Different testing specimens with the loading axes along 0° (rolling direction, RD), 22.5° , 45° , 67.5° , and 90° (normal direction, ND) with respect to the RD were machined from a rolled plate with a thickness of 76.2 mm. The material has been experimentally investigated by Wang et al. (2020e). As shown in Fig. 2, the initial texture of the material is a very strong basal texture with the c-axes of most grains aligning parallel to the ND, and $\{10-10\}$ pole figure shows a uniformly distributed prismatic planes in the RD-TD (transverse direction) plane. The initial texture is discretized as 6740 different orientations with equal volume fractions for all simulations. The plastic deformation is assumed to be accommodated by prismatic ($\{10-10\}\langle 11-20\rangle$), basal ($\{0001\}\langle 11-20\rangle$), pyramidal $\langle c+a \rangle$ ($\{11-22\}\langle 11-23\rangle$) slips, and $\{10-12\}\langle 10-11\rangle$ tensile twinning as well as $\{10-11\}\langle 10-12\rangle$ compressive twinning. The room temperature elastic constants of Mg single crystal are taken to be (GPa) $C_{11} = 59.5$, $C_{12} = 26.1$, $C_{13} = 21.8$, $C_{33} = 65.6$ and $C_{44} = 16.3$ (Slutsky and Garland, 1957). In addition, the Affine self-consistent scheme is employed for all simulations (Wang et al., 2010a; Qiao et al., 2015a). The loading (strain) rate is set to be $8 \times 10^{-4} \text{ s}^{-1}$ according to Wang et al. (2020e). The reference slip/twinning rate, $\dot{\gamma}_0$, and the rate sensitivity, m , are set to be the same for all the slip/twinning systems: $\dot{\gamma}_0 = 8 \times 10^{-4} \text{ s}^{-1}$ and $m = 0.05$.

It is known that the strain rate dependency induced by Eq. (2) potentially affects the predicted mechanical behavior of Mg alloys deformed at room temperature. From a numerical point of view, very low rate sensitivity (e.g., $m \ll 0.05$) will cause numerical difficulties in rate sensitive constitutive models. Therefore, the rate sensitivity parameter, $m = 0.05$, is commonly used to facilitate easy convergence in such crystal plasticity-based models, including the VPSC (e.g., Maldar et al., 2020; Zecevic et al., 2020), EVPSC (e.g., Ma et al., 2019; Wang et al., 2020f; Guo et al., 2021), and some CPFE models (e.g., Hama et al., 2018; Briffod et al., 2019; Jalili et al., 2020; Zhang et al., 2021a). To model nearly rate insensitive materials, some studies set the reference shear rate equal to the imposed strain rate (Kok et al., 2002; Knezevic et al., 2013, 2016; Zhao et al., 2019; Qiao et al., 2021). By doing so, the rate sensitivity m is no longer physically meaningful but allows easy convergence (Chapuis and Liu, 2018), however, the parameter m is still involved in solving non-linear governing equations, and so the dependency of mechanical behavior on the parameter m cannot be ignored especially with relatively high rate-sensitivity (e.g., $m > 0.1$). Recently, an adaptive time stepping scheme (Wu et al., 1996) was used by Wang et al. (2018) in the EVPSC model to enhance its numerical robustness for very low rate sensitivity. In this study, high number of loading cycles will cause extremely long computation time even with the improved version of EVPSC model, so we still choose to set the reference shear rate equal to the applied loading rate with the parameter $m = 0.05$ for all simulations, as a compromise between computational efficiency and accuracy.

3.1. Monotonic loading

In this Subsection, the monotonic stress-strain responses in different material orientations of the AZ31B plate is numerically investigated. The Voce-type hardening law parameters for various deformation modes could be mainly determined by curve-fitting the calculated stress-strain curves to corresponding experimental data, and in order to appropriately mimic the mechanical response under cyclic loadings, cyclic loading experiments should also be accounted for in determining some of these parameters. Discussions in this aspect will be addressed in subSection 3.2.1. Table 1 lists the obtained parameters for the current model. It is noted that the initial CRSS of detwinning is set to be different from twinning, $\tau_{0C}(\tau_{0D})=0.5\tau_{0A}(\tau_{0B})$, while the other hardening parameters are kept the same for twinning and detwinning. Detwinning is not activated during monotonic loadings and so the material parameters associated with detwinning will be discussed in Section 3.2.

Fig. 3 presents the measured (symbols) and fitted (lines) stress-strain curves under monotonic tension and compression for the different material orientations. It is clear that the calculated stress-strain curves for tension and compression along all the material orientations concerned are generally in good agreement with experimental data. It is also observed that the current model slightly overestimates the experimental data under monotonic compression for the 0° (RD) and 22.5° material orientations (Figs. 3a and b) while underestimates the measured stress-strain curves at the early stage of deformation under tension for the 67.5° and 90° (ND) material orientations (Figs. 3e and f). In addition, for the 45° material orientation, a relatively less agreement could be found between

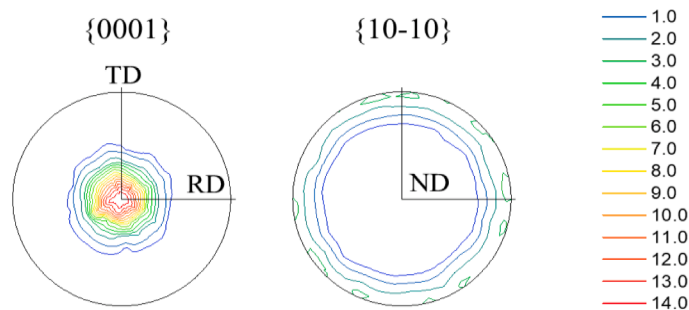


Fig. 2. Initial texture of the rolled AZ31B plate in terms of $\{0001\}$ and $\{10-10\}$ pole figures.

Table 1

List of material parameters for the EVPSC-TDT model. The parameter $h^{\alpha\beta}$ denotes latent hardening effect of the slip/twin mode β upon the other deformation mode α .

Mode	τ_0 (MPa)	τ_1 (MPa)	h_0 (MPa)	h_1 (MPa)	$h^{\alpha\beta}$	A_1	A_2
Basal	14	15	180	0	2.0		
Prismatic	82	55	380	0	0.2		
Pyramidal	90	115	1600	0	1		
Extension twin	$\tau_{0A} (\tau_{0B})=27$ $\tau_{0C} (\tau_{0D})=13.5$	20	50	0	1	0.60	1.15
Compression twin	148	60	250	0	1	0.35	0.00

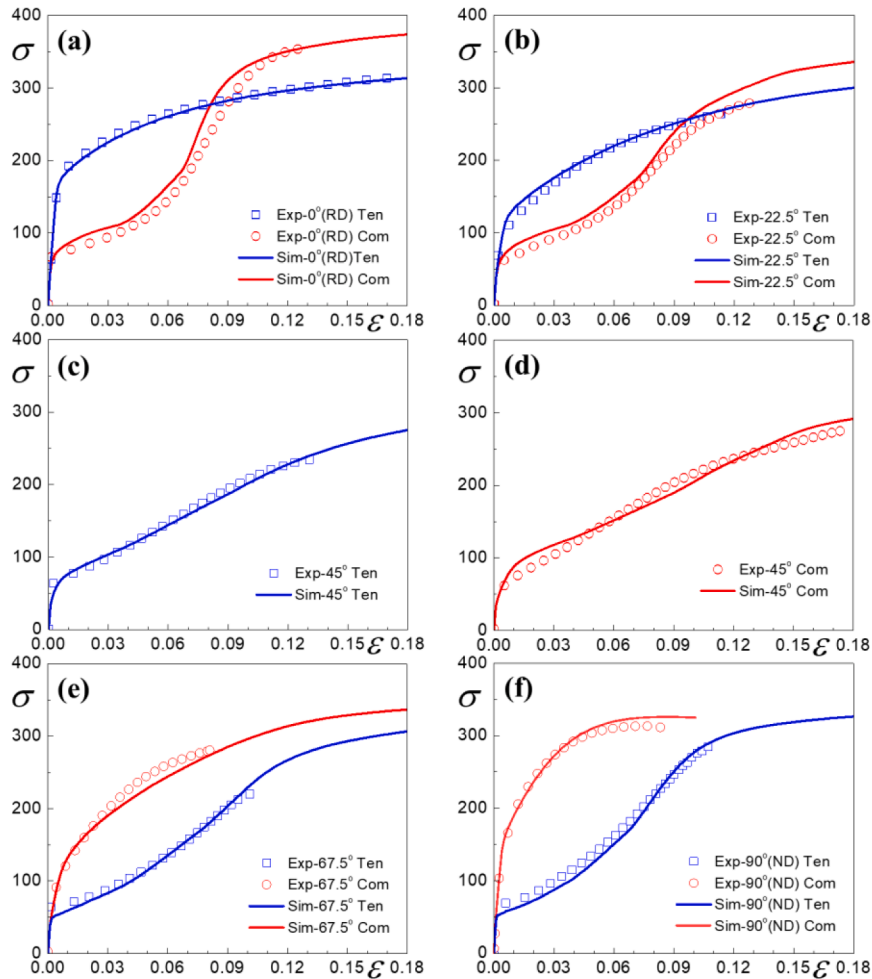


Fig. 3. Measured (symbols) and fitted (lines) stress-strain curves under monotonic tension and compression for the material orientations of 0° (RD) (a), 22.5° (b), 45° (c and d), 67.5° (e) and 90° (ND) (f).

the simulation and corresponding compression test (Fig. 3d).

Fig. 4 shows the predicted relative activities under monotonic tension and compression for the material orientations of 0° (RD), 45° and 90° (ND). For tension along the RD (Fig. 4a), prismatic and basal slips dominate plastic deformation with prismatic slip being the major contributor, and tensile twinning is almost not activated during deformation due to the initial strong basal texture. For the 45° material orientation (Fig. 4b), prismatic slip is strongly constrained at the early stage of deformation, and tensile twinning becomes active and acts as a complement to the primary basal slip. For tension along the ND (Fig. 4c), tensile twinning becomes most active and it dominates plastic deformation together with basal slip up to the strain of ~ 0.03 , after that prismatic slip starts to contribute to the deformation and increases with the decrease of tensile twinning and finally becomes the most active deformation mode after the strain of ~ 0.08 , which is caused by the accumulation of twinned grains that favor the activation of prismatic slip. In addition, the predicted tensile twin VFs at large strains under tension for the 0°, 22.5°, 45°, 67.5° and 90° (ND) material orientations are

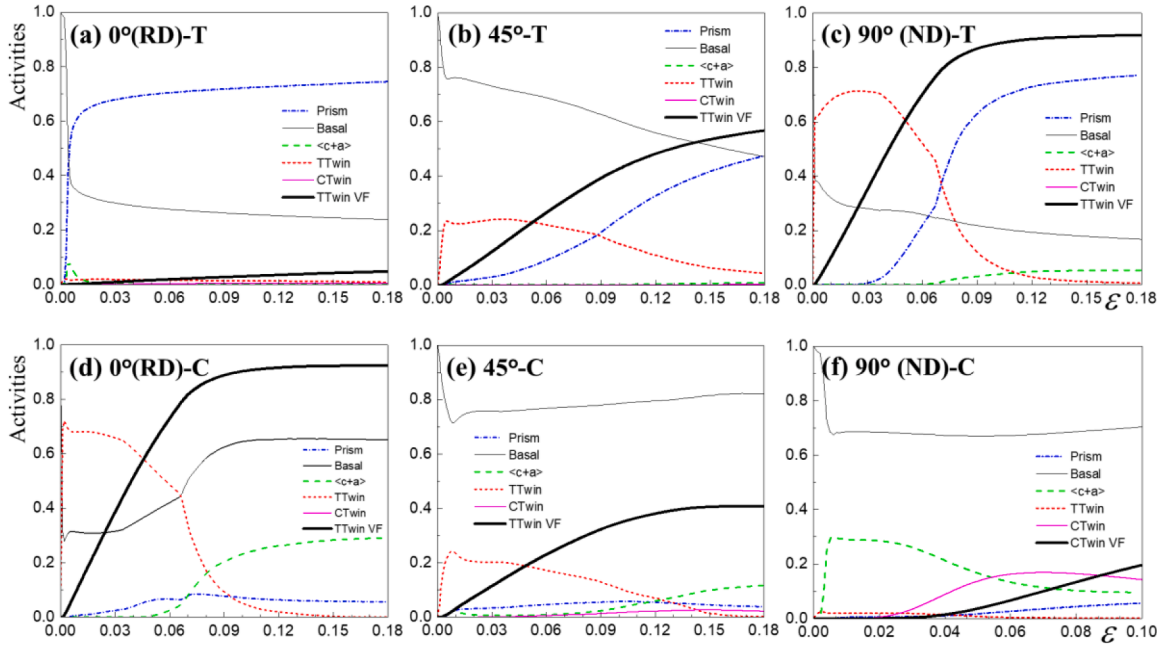


Fig. 4. Predicted relative activities under monotonic tension and compression for the material orientations of 0° (RD) (a and d), 45° (b and e) and 90° (ND) (c and f). Symbols of “T” and “C” denote tension and compression, respectively.

$\sim x223C0.048$, $\sim x223C0.28$, $\sim x223C0.55$, $\sim x223C0.87$ and $\sim x223C0.92$, respectively.

For compression along the RD, Fig. 4d shows that tensile twinning dominates plastic deformation up to the strain of $\sim x223C0.06$, and after that basal slip becomes the most dominant deformation mode, in addition, pyramidal slip starts to increasingly accommodate plastic deformation with the accumulation of twinned grains having their c -axes approximately aligned to the compressive axis, which causes a rapid strain hardening rate (Wu et al., 2017). For the 45° material orientation (Fig. 4e), the activity of tensile twinning decreases much more compared with that under compression along the RD and so basal becomes much more active to contribute to plastic deformation. For compression along the ND (Fig. 4f), pyramidal $\langle c + a \rangle$ increases rapidly with decreasing the activity of basal slip at the very early deformation stage. Compressive twinning is observed to be activated at the strain of $\sim x223C0.02$ and the predicted compressive twin VF reaches $\sim x223C0.2$ at the strain of 0.10. Furthermore, numerical results show that the predicted tensile twin VFs under compression for the 0°, 22.5°, 45°, 67.5° and 90° (ND) material orientations can respectively reach $\sim x223C0.92$, $\sim x223C0.75$, $\sim x223C0.41$, $\sim x223C0.1$ and $\sim x223C0.02$ at large strains.

The above results indicate that the EVPSC-TDT, with a single set of material parameters, permits predictions of the strength anisotropy and the strain hardening behavior under monotonic loading along all five orientations involving cases in which the contribution of twinning is dominated, negligible and intermediate, which further supports the findings by Guo et al. (2015). It is important to point out that the work performed by Guo et al. (2015) and reported in this section is only for monotonic loading, where detwinning is not observed. The present work aims to study, by using the EVPSC-TDT model, the stabilized plastic deformation behavior of a rolled AZ31B plate under fully reversed cyclic loading in five different material orientations with respect to the RD on the RD-ND plane at three different strain amplitudes. For the total of 15 cases of cyclic loading considered in the present work, detwinning plays a critical role and will be investigated in the following section.

3.2. Cyclic loading

In this Section, we will numerically study the cyclic stabilized plastic response of the rolled AZ31B plate in different material orientations. As mentioned before, twinning and detwinning alternately contribute to plastic deformation during the fully reversed cyclic loading with relatively large strain amplitudes (e.g., 2%, 3%, and 4% in this study). Residual twins will accumulate during the twinning-detwinning associated cyclic deformation, and Eq. (5) is used here to describe the process of residual twinning. The effect of the material parameter governing the rate of saturation of residual twins, b_{tw}^{α} , and the saturated VF of residual twin, f_{sat}^{α} , on plastic deformation will be discussed in this Section. In addition, based on the direct observation of twinning-detwinning-retwinning on Mg single crystal under cyclic tension-compression in [0001] direction, Yu et al. (2011) concluded that residual twins accumulate with increasing loading cycles resulting in the reduced activities for fresh twins, retwinning and detwinning, and the twin area at the current tensile peak stress is only slightly increased compared with that at the previous tensile peak stress. Therefore, we introduce a threshold equation with a parameter, q , to constrain the fresh twinning and retwinning,

$$f_{(k+1)T}^{sh,\alpha} = f_{kT}^{\alpha} + q(f_{res(k)Dr}^{\alpha} - f_{res[(k-1)Dr]}^{\alpha}) \quad (0 < q \leq 1, k \geq 2) \quad (9)$$

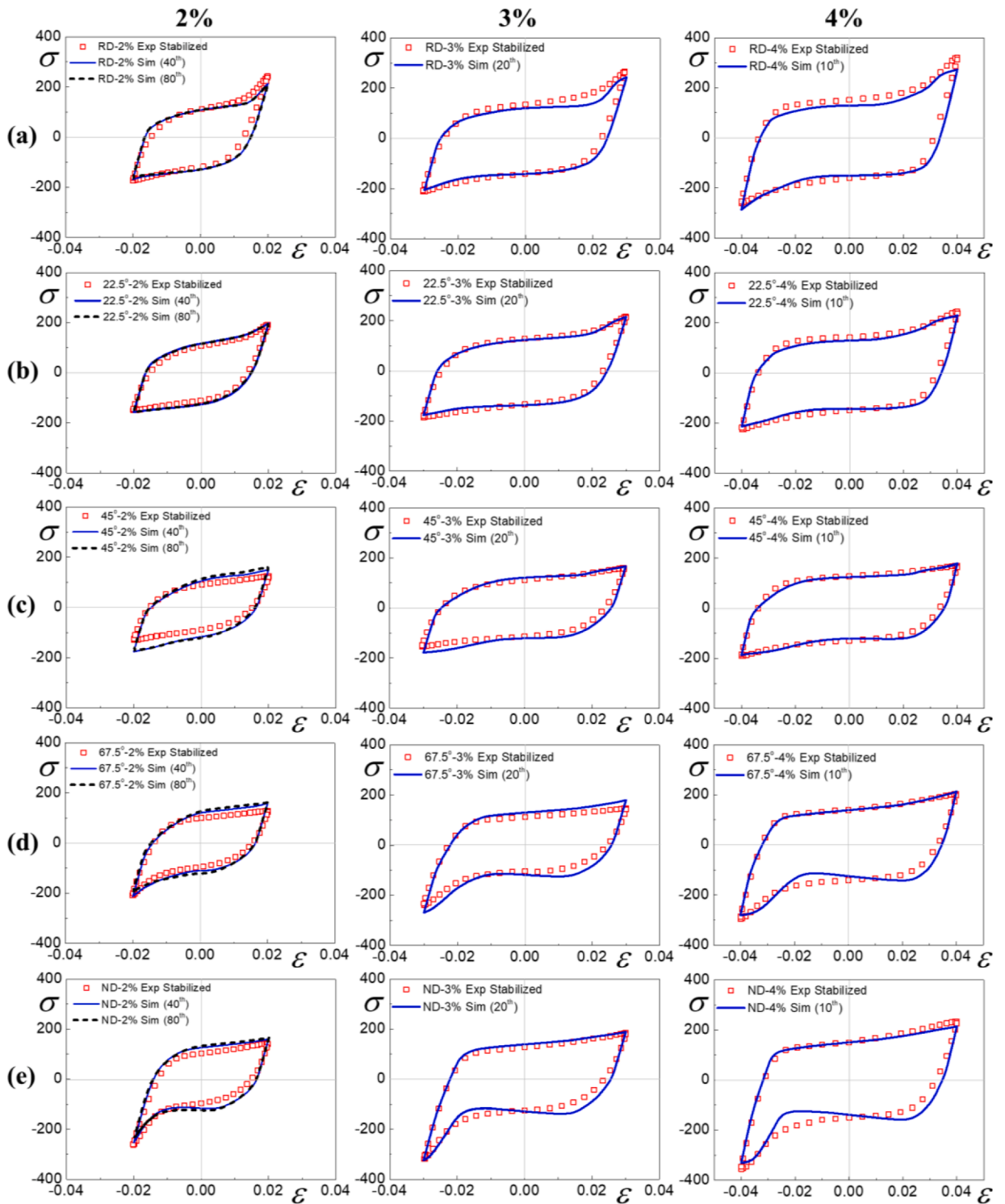


Fig. 5. Measured (symbols) and calculated (lines) stabilized stress-strain hysteresis loops under cyclic loadings in the material orientations of 0° (RD) (a), 22.5° (b), 45° (c), 67.5° (d) and 90° (ND) (e) at various strain amplitudes of 2%, 3%, and 4%. The dashed lines are the calculated stress-strain curves at the 80th cycle for 2% strain amplitude.

where f_{kT}^α denotes the twin VF for twin system α at the end of twinning during the k^{th} twinning-detwinning pair, and $f_{res(kDt)}^\alpha$ is the residual twin VF for twin system α at the end of detwinning during the k^{th} twinning-detwinning pair. $f_{(k+1)T}^{th,\alpha}$ is the threshold value of twin VF for twin system α during the twinning process within the $(k + 1)^{th}$ twinning-detwinning pair. It is assumed that twin system α will be terminated once the twin VF of the twin system reaches its threshold value as described by Eq. (9).

It is very important to distinguish the k^{th} twinning-detwinning pair and the k^{th} loading cycle. A twinning-detwinning pair is defined as a process of twinning and subsequent detwinning, but before next twinning occurs. A loading cycle is defined as a process of straining from a designed peak (e.g., $\epsilon = 0.02$, see Fig. 6b), unloading and reversal loading to its maximum value ($\epsilon = -0.02$), and reloading to the peak ($\epsilon = 0.02$). It is important to keep in mind that in reality (i.e., in experimenting) a cycle is accounted even when loading and reversal loading do not reach their designed peaks due to difficulties involved in controlling process.

It should also be noted that the parameters f_{sat}^α , b_{tw}^α , and q are determined based on the measured stabilized stress-strain responses of the 45° and 90° (ND) material orientations, and the determined parameters ($f_{sat}^\alpha = 0.035$, $b_{tw}^\alpha = 0.05$, and $q = 0.5$) will be employed in all simulations of the AZ31B plate under cyclic loadings if not specified otherwise.

3.2.1. Stabilized stress-strain response

The experimental study by Wang et al. (2020e) suggested that two kink points exist in the strain-life fatigue curve of any given material orientation of the AZ31B plate and twinning-detwinning could be obviously observed to occur during cyclic loading when the strain amplitude is higher than the higher kink point. Therefore, in order to focus on the twinning and detwinning behavior of the AZ31B plate, we constrain our attention on the cyclic plastic response of the AZ31B plate with only relatively large strain amplitudes (e.g., 2%, 3%, and 4%) in this study. In addition, the fatigue experiments also indicated that the number of loading cycles to failure for 2% strain amplitude of each material orientation is less than 100, and it decreases with the increase of strain amplitude with it being less than 10 for the strain amplitude of 4%. So, for simplicity, we only run the simulations up to 10th and 20th cycles for the study of stabilized plastic response of each material orientation with strain amplitudes of 4% and 3%, respectively. For the strain amplitude of 2%, only the calculated stress-strain curves up to 40th cycle will be reported thereafter if not specified.

Fig. 5. shows the measured (symbols) and calculated (lines) stabilized stress-strain hysteresis loops for each material orientation under cyclic loading with strain amplitudes of 2%, 3%, and 4%. It can be seen that the current model can generally capture the main features of the stabilized stress-strain hysteresis loops associated with twinning and detwinning. For the 0° material orientation (Fig. 5a), the measured upper branches of the stress-strain hysteresis loops are underestimated from the strain of 0 to 2.0% especially for the strain amplitudes of 3% and 4% where detwinning is gradually saturated with the increase of non-basal slips. For the 22.5° material orientation (Fig. 5b), the predicted stabilized stress-strain hysteresis loops are in good agreement with the corresponding

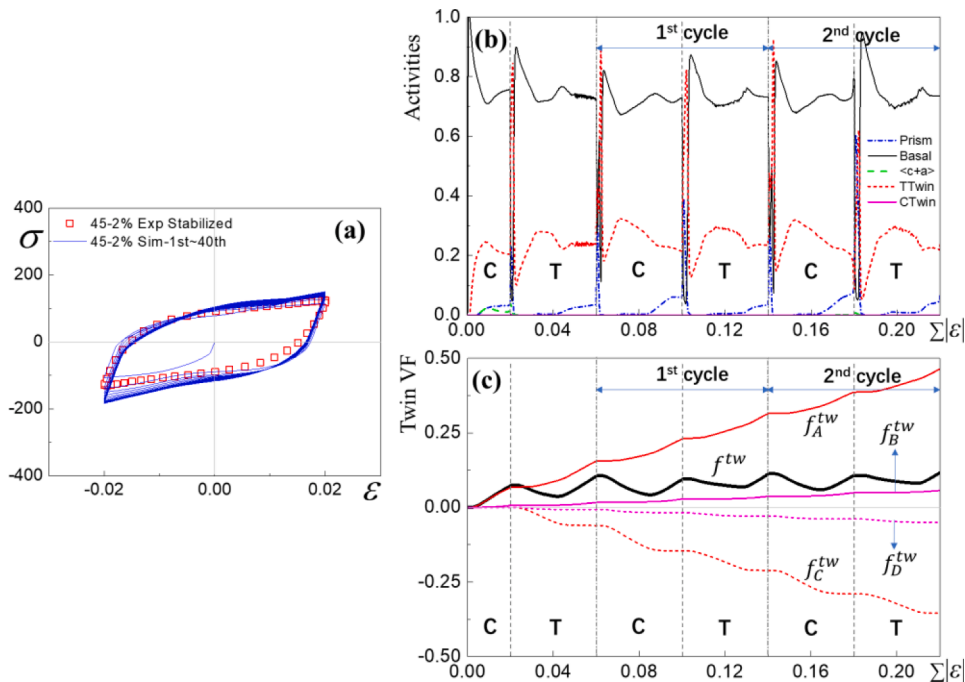


Fig. 6. Measured stabilized (symbols) stress-strain hysteresis loop and calculated (lines) stress-strain curves under cyclic loading up to 40th cycles for the 45° material orientation at 2% strain amplitude (a) the predicted relative activities (b) and twin volume fractions (c) versus the accumulated strain. Symbols of ‘C’ and ‘T’ denote compression and tension, respectively. f_A^{tw} , f_B^{tw} , f_C^{tw} , and f_D^{tw} respectively represent twin VF for operations A, B, C, and D. f^{tw} is the total twin VF.

measured data. For the 45° material orientation (Fig. 5c), the current model could predict the measured stabilized hysteresis loops for strain amplitudes of 3% and 4% while both the upper and lower branches for strain amplitude of 2% are overestimated. For the 67.5° and 90° (ND) material orientations (Figs. 5d and 5e), the current model overestimates the upper branch of the stress-strain hysteresis loop for strain amplitude of 2% where twinning and basal slip dominates the plastic deformation during tension loading reversal, and for strain amplitudes of 3% and 4%, the measured lower branches of the stress-strain hysteresis loops are not well predicted which is caused by the predicted later start and completion of detwinning and will be discussed in Section 3.2.5. From Fig. 5, it is also seen that the predicted stress-strain hysteresis loop at the 40th loading cycle for each material orientation with strain amplitude of 2% is almost overlapped with that at the 80th loading cycle and so it is enough to represent the calculated stabilized stress-strain hysteresis loop.

For closer examination of discrepancies between the calculated and measured stabilized plastic response for the 45° material orientation at 2% strain amplitude, we present in Fig. 6 the measured stabilized (symbols) stress-strain curve and calculated (lines) cyclic stress-strain curves up to 40th cycle for the material orientation, and the predicted relative activities as well as twin VFs up to 2nd cycle. In Fig. 6, f^{tw} denotes the evolution of the net twin VF of the aggregate. f_A^{tw} and f_B^{tw} are the accumulated twin VFs for operations A and B while f_C^{tw} and f_D^{tw} represent the accumulated VFs of detwinning for operations C and D. It is seen that, from Fig. 6b, basal slip and tensile twinning are the most and second active deformation modes, respectively. Prismatic slip increases with the decrease of tensile twinning during the late stage of each tension and compression reversals. Closer inspection of simulation results indicates that prismatic slip at tensile peaks gradually increases with the increase of loading cycles up to around 20th cycle and then stays almost unchanged while that at compressive peaks only increases with the increase of loading cycles up to ~x223C10th cycle, which causes the observed cyclic hardening at the tensile and compressive peaks. Fig. 6c shows that only tensile twinning occurs during the first compression to strain of -2%, and then twinning and detwinning simultaneously occurs during each of the following tension/compression reversals. The total calculated twin VF at the 40th tensile peak reaches about ~x223C0.185 indicating the limited twinning for the 45° material orientation as pointed out by Wang et al. (2020e).

It is worth mentioning here that the overestimation of the measured stabilized stress-strain hysteresis loop for the 45° material orientation is closely related to the applied latent hardening coefficients for basal and prismatic slips due to tensile twinning. However,

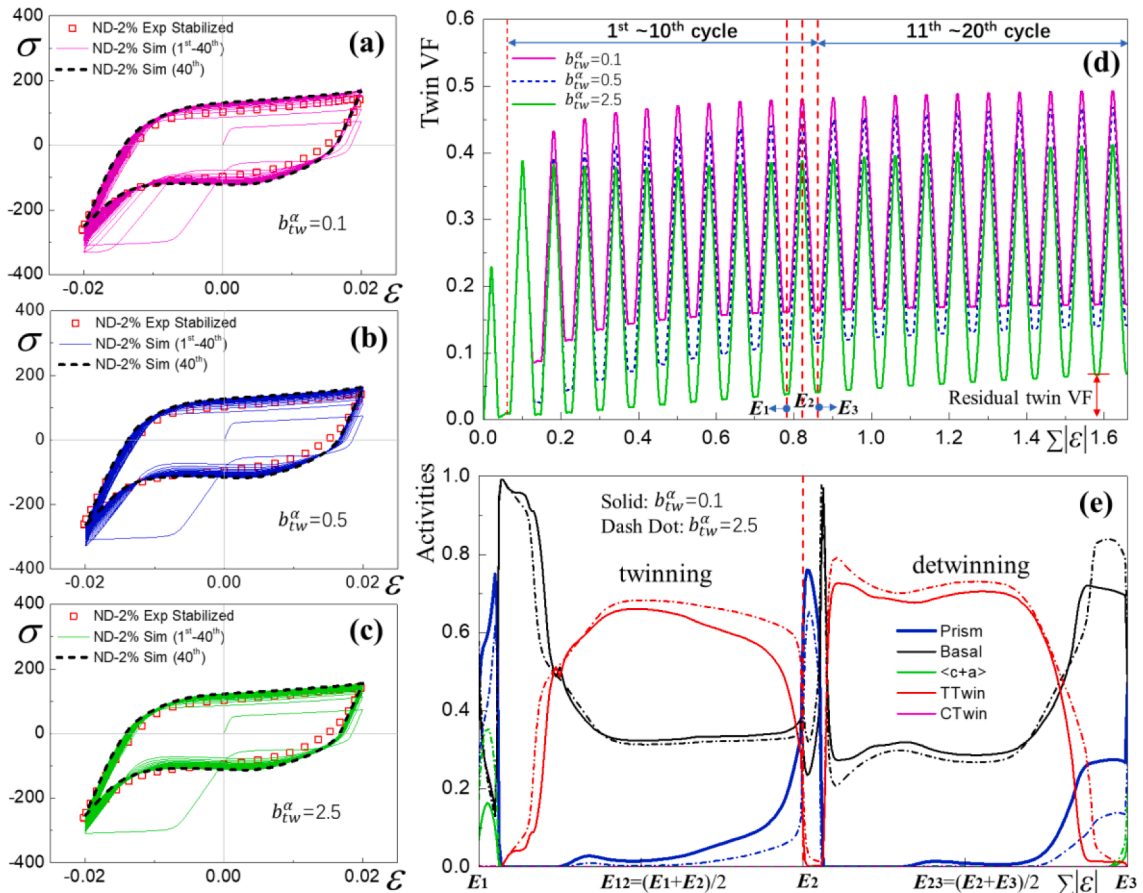


Fig. 7. Measured stabilized (symbols) stress-strain hysteresis loop and calculated (lines) stress-strain curves under cyclic loading up to 40th cycle for the 90° (ND) material orientation at 2% strain amplitude for $b_{tw}^\alpha = 0.1$ (a), $b_{tw}^\alpha = 0.5$ (b) and $b_{tw}^\alpha = 2.5$ (c). The predicted twin VFs for the three cases (d) as well as the predicted relative activities of the 10th loading cycle for $b_{tw}^\alpha = 0.1$ and $b_{tw}^\alpha = 2.5$ (e). The dashed lines in (a), (b), and (c) are the calculated stress-strain curves at the 10th cycle.

further decrease of the current latent hardening parameters (2 for basal slip and 0.2 for prismatic slip, see Table 1) will deteriorate other predictions. In addition, numerical tests show that obvious overestimation of cyclic hardening appears if we assign a high latent hardening parameter for twin-twin interaction to balance monotonic tension along the ND and compression along the RD/TD as did in previous works (Zhao et al., 2019; Guo et al., 2021; Qiao et al., 2021), therefore, in this study the latent hardening parameter for twin-twin interaction is still set to be the default value of 1. It is also worth mentioning that, to avoid unexpected cyclic hardening, the asymptotic hardening rate, h_1^α , of the extended Voce law (see, Eq. (6)) for each deformation mode should be set to be zero. In summary, to appropriately mimic the cyclic deformation mechanisms of Mg alloys based on crystal plasticity-based models (e.g., EVPSC), cyclic loading experiments should also be accounted for along with the measured monotonic loadings to determine the material parameters especially for the latent hardening parameters. The importance of experimental cyclic stabilized stress-strain hysteresis loops in determining the material parameters in phenomenological constitutive modeling was previously pointed out by Roostaei and Jahed (2018).

3.2.2. Effect of b_{tw}^α

To investigate the effect of the material parameter, b_{tw}^α , governing the saturation rate of residual twins on the stabilized plastic response, Fig. 7 shows the cyclic stress-strain response for the ND material orientation at strain amplitude of 2% with various b_{tw}^α values, and the predicted twin VF evolution with the accumulated strain up to 20th cycle as well as the predicted relative activities of the 10th cycle. From Fig. 7d, it is seen that the residual twin VF decreases with the increase of b_{tw}^α from 0.1 to 2.5 at each compressive peak. Closer examination indicates that for the case of $b_{tw}^\alpha = 0.1$, the residual twin VF increases sharply during the first few loading cycles and saturates around the 20th loading cycle with twin VF being $\sim x223C0.5$ at the tensile peak and residual twin VF being $\sim x223C0.17$ at the compressive peak. For the case of $b_{tw}^\alpha = 0.5$, the residual twin saturates at $\sim x223C80$ th cycle with residual twin VF being the same as the saturated value of $\sim x223C0.17$ for $b_{tw}^\alpha = 0.1$. For the case of $b_{tw}^\alpha = 2.5$, the residual twin VF at the compressive peak of the

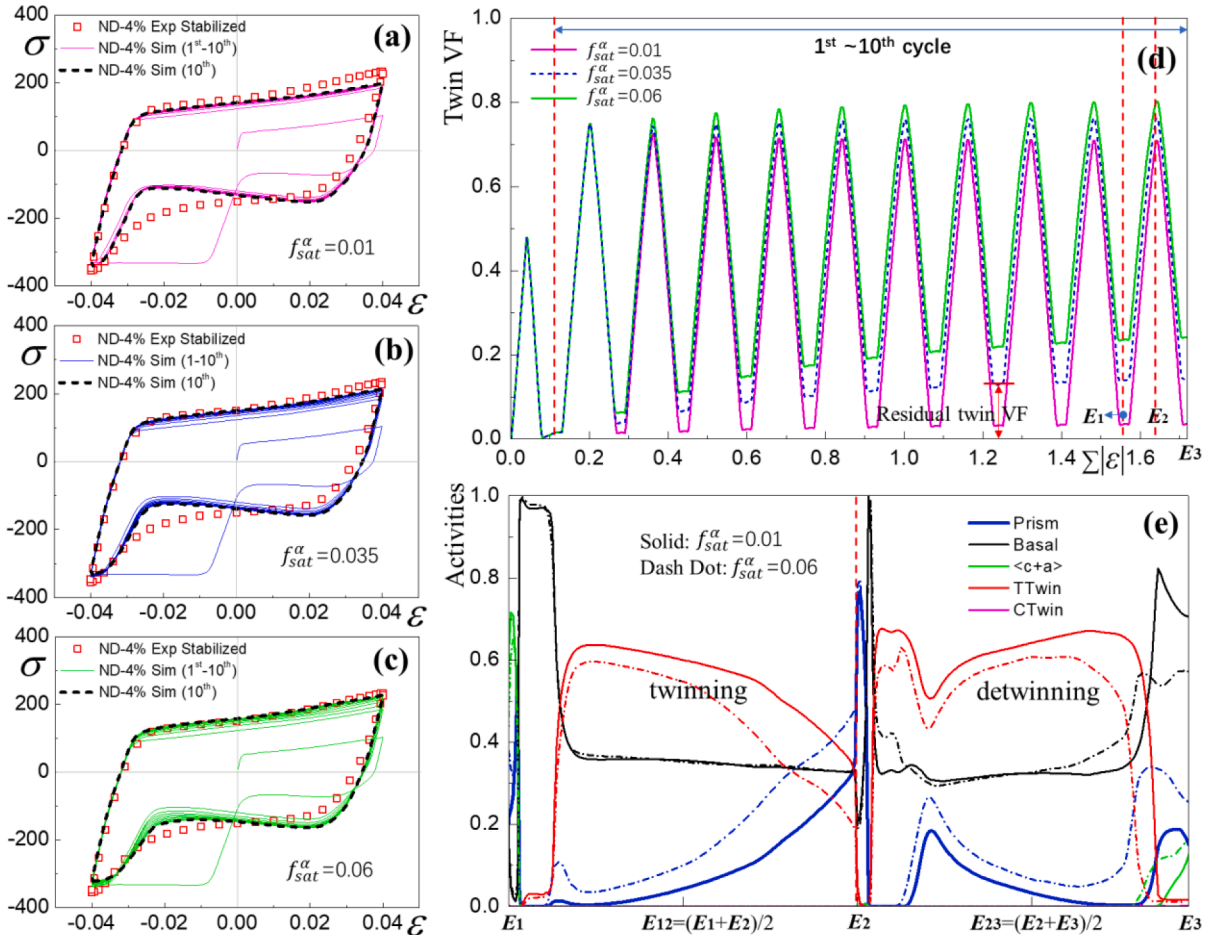


Fig. 8. Measured stabilized (symbols) stress-strain hysteresis loop and calculated (lines) stress-strain curves under cyclic loading up to 10th cycle for the 90° (ND) material orientation at 4% strain amplitude for $f_{sat}^\alpha = 0.01$ (a), $f_{sat}^\alpha = 0.035$ (b) and $f_{sat}^\alpha = 0.06$ (c). The predicted twin VFs for the three cases (d) as well as the predicted relative activities of the 10th loading cycle for $f_{sat}^\alpha = 0.01$ and $f_{sat}^\alpha = 0.06$ (e). The dashed lines in (a), (b), and (c) are the calculated stress-strain curves at the 10th cycle.

40th loading cycle only reaches $\sim x223C0.1$, and so much more loading cycles are needed to reach saturation. In addition, it is worth noting that the twin VF at each tensile peak is also correlated to the parameter b_{tw}^α through Eq. (9), which is also reflected in Fig. 7d.

Fig. 7e presents the predicted relative activities during the 10th loading cycle (E_1 to E_3). It is clear that prismatic slip increases with the decrease of tensile twinning during tension reversal from E_{12} to E_2 . It is also seen that prismatic slip is more active for $b_{tw}^\alpha = 0.1$ than for $b_{tw}^\alpha = 2.5$ as more residual twins could be created at the previous compressive peak for $b_{tw}^\alpha = 0.1$ than for $b_{tw}^\alpha = 2.5$. Closer examination shows that the relative activities of various deformation modes at the 40th loading cycle exhibit similar trend with those at the 10th loading cycle. Therefore, overestimation of the upper branch of the measured stabilized stress-strain hysteresis loop during tension reversal from the strain of 0 to 2% is expected to be stronger for $b_{tw}^\alpha = 0.1$ than for $b_{tw}^\alpha = 2.5$ (see dotted lines in Figs. 7a and c). Fig. 7e also shows that detwinning is observed to decrease with the increase of prismatic slip during compression reversal from E_{23} to E_3 , and prismatic slip is also more active for $b_{tw}^\alpha = 0.1$ than for $b_{tw}^\alpha = 2.5$. In addition, pyramidal slip is found to be activated near the compression peak for both $b_{tw}^\alpha = 0.1$ and $b_{tw}^\alpha = 2.5$ with relatively stronger activity for $b_{tw}^\alpha = 2.5$, although not so obvious. It is interesting that the discrepancies in activities for the concerned cases do not cause apparent changes in the lower branches of the predicted stabilized stress-strain hysteresis loops, however, the predicted stress-strain responses during each compression reversal of the first few loading cycles are quite different. It is thus clear that the lower the parameter b_{tw}^α is, the higher the saturation rate of residual twins is. The higher saturation rate of residual twins for $b_{tw}^\alpha = 0.1$ could cause the earlier transition from detwinning to non-basal (prismatic) slip during the late stage of compression reversal of a given loading cycle and so lead to higher strain hardening compared with the case of $b_{tw}^\alpha = 2.5$ (Figs. 7a-c). Moreover, the cyclic plastic response of the material orientation for $b_{tw}^\alpha = 0.5$ lies between those for $b_{tw}^\alpha = 0.1$ and $b_{tw}^\alpha = 2.5$.

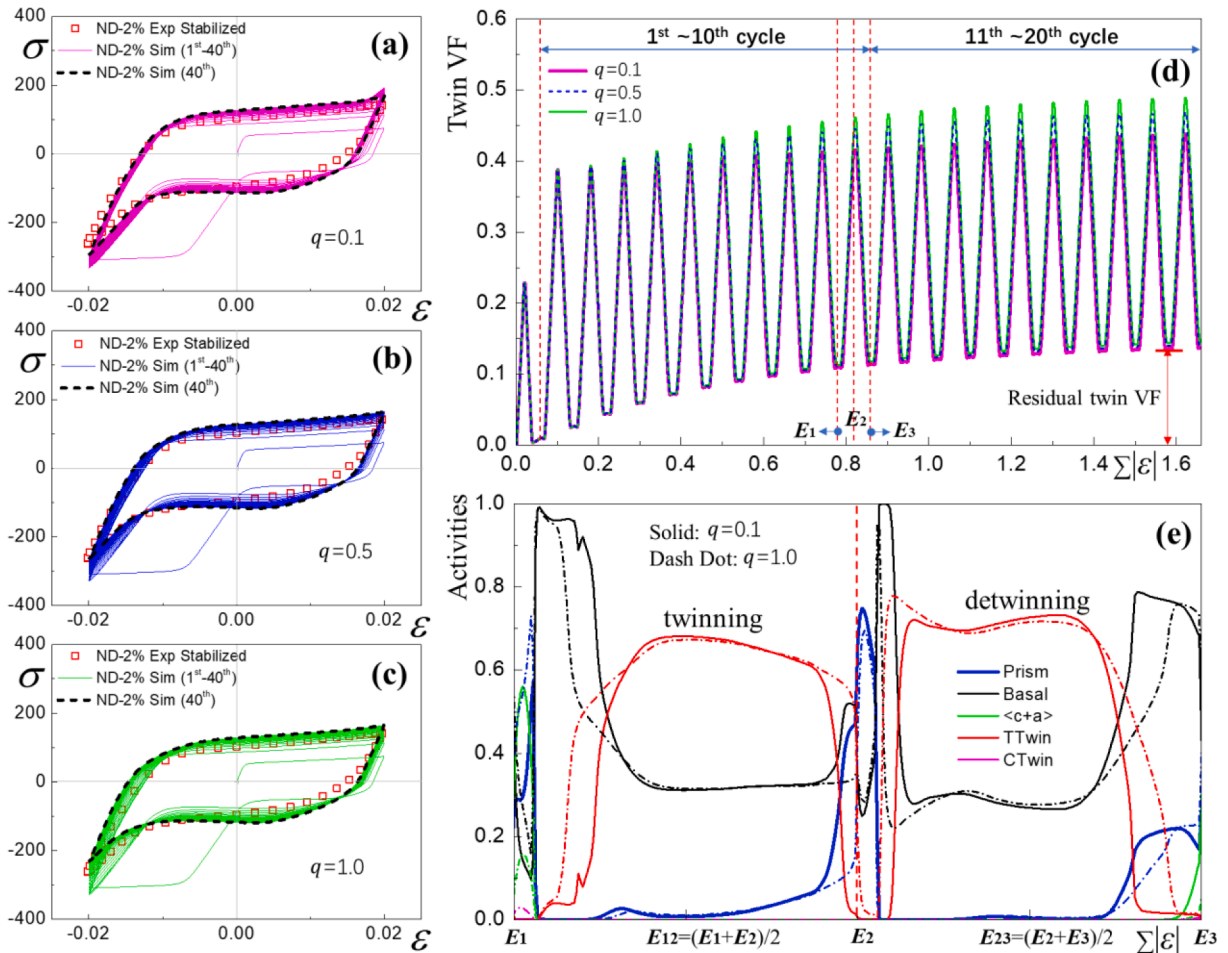


Fig. 9. Measured stabilized (symbols) stress-strain hysteresis loop and calculated (lines) stress-strain curves under cyclic loading up to 40th cycle for the 90° (ND) material orientation at 2% strain amplitude for $q=0.1$ (a), $q=0.5$ (b) and $q=1.0$ (c). The predicted twin VFs for the three cases (d) as well as the predicted relative activities of the 10th loading cycle for $q=0.1$ and $q=1.0$ (e). The dashed lines in (a), (b), and (c) are the calculated stress-strain curves at the 40th cycle.

3.2.3. Effect of f_{sat}^α

In this Subsection, the effect of the saturated residual twin VF, f_{sat}^α , on cyclic stabilized plastic response of the ND material orientation at strain amplitude of 4% is to be investigated. Fig. 8 gives the calculated cyclic stress-strain curves up to 10th loading cycle with measured stabilized stress-strain hysteresis loop being included for comparison, and the predicted twin VF for three cases of $f_{sat}^\alpha = 0.01$, $f_{sat}^\alpha = 0.035$, and $f_{sat}^\alpha = 0.06$ as well as the predicted relative activities for the 10th loading cycle. From Fig. 8d, it is seen that the predicted residual twin VF at each compression peak gradually increases with the loading cycles and it reaches the values of $\sim x223C0.038$, $\sim x223C0.14$, and $\sim x223C0.24$ at the 10th loading cycle for the cases of $f_{sat}^\alpha = 0.01$, $f_{sat}^\alpha = 0.035$, and $f_{sat}^\alpha = 0.06$, respectively. The predicted twin VF at the tension peak of the 10th loading cycle slightly increases with the increase of b_{tw}^α from 0.01 to 0.06 and reaches $\sim x223C0.70$, $\sim x223C0.75$, and $\sim x223C0.80$, respectively for the three cases. In addition, based on Eq. (9) and the definition of macroscopic loading cycle, it can be inferred that the incremental twin VF of the aggregate between two neighboring tension peaks of the macroscopic loading cycle can be related to the incremental residual twin VF between two neighboring compression peaks by $\Delta f_N \leq q(\Delta f_{res(N)})$. Based on simple derivation, the predicted twin VF at the tension peak of the 10th cycle for the three cases should be respectively less than 0.76, 0.81, and 0.86 ($f_{10} \leq f_1 + 0.5f_{res(9)} \approx 0.74 + 0.5f_{res(9)}$). Therefore, it seems that the implementation of Eq. (9) in the current model is reliable in this respect.

From Fig. 8e, it can be found that prismatic slip gradually increases with decrease of tensile twinning during the tension reversal of 10th loading cycle and it is predicted to be more active for $f_{sat}^\alpha = 0.06$ than for $f_{sat}^\alpha = 0.01$, which results in stronger strain hardening effect during tension reversal from strain of zero to 4% for $f_{sat}^\alpha = 0.06$ compared with that for $f_{sat}^\alpha = 0.01$ (Figs. 8a and c). Fig. 8e also indicates that prismatic slip needs to be activated at the early stage of the compression reversal to accommodate plastic deformation, and then decreases rapidly with increasing the VF of detwinning which reorients the twinned grains formed at the previous tensile peak back to their parent matrix orientation. With the saturation of detwinning at the very late stage of compression reversal, prismatic slip turns stronger again to accommodate plastic deformation with pyramidal slip also being activated. In addition, as expected, prismatic slip is found to be more active during the compression reversal for $f_{sat}^\alpha = 0.06$ than for $f_{sat}^\alpha = 0.01$ leading to stronger strain hardening effect especially at the late stage of the compression reversal (see, Fig. 8a and c). It is noted that better prediction of measured stabilized stress-strain hysteresis loop for the ND material orientation with 4% strain amplitude could be obtained by setting the parameter f_{sat}^α to be $f_{sat}^\alpha = 0.06$, however, other simulation results where prismatic slip also matters (e.g., cyclic loading for the ND material orientation with 2% strain amplitude) will be deteriorated.

3.2.4. Effect of q

As mentioned before, we introduce a threshold equation with a parameter, q , to constrain the fresh twinning and retwinning in the current model. The effect of the parameter on cyclic plastic response will be investigated for the 90° (ND) material orientation at strain amplitude of 2%. Fig. 9 presents the calculated cyclic stress-strain responses with various q values ($q = 0.1, 0.5, \text{ and } 1.0$) and the predicted twin VF evolution with the accumulated strain up to 20th cycle as well as the predicted relative activities for the 10th cycle. From Fig. 9d, it is found that the residual twin VFs at each compression peak for all three cases concerned are almost the same during the first ten loading cycles, and closer examination shows that the differences slightly increase with further cyclic loading and the residual twin VFs at the 40th loading cycle for the three cases ($q = 0.1, 0.5, \text{ and } 1.0$) are $\sim x223C0.152$, $\sim x223C0.158$, and $\sim x223C0.164$, respectively. Such small discrepancies should be caused by different accumulated twin VFs for these cases although the other two parameters b_{tw}^α and f_{sat}^α are kept unchanged (see Eq. (5)). The twin VFs at the tensile peak of the 40th loading cycle for the three cases ($q = 0.1, 0.5, \text{ and } 1.0$) are predicted to be $\sim x223C0.46$, $\sim x223C0.47$, and $\sim x223C0.5$, respectively. According to the subSection 3.2.3, the predicted twin VF at the tension peak of the 40th cycle for the three cases should be respectively less than 0.41, 0.47, and 0.55 ($f_{40} \leq f_1 + qf_{res(39)} \approx 0.39 + qf_{res(39)}$), however, for the case of $q = 0.1$, the predicted twin VF, f_{40} , does not follow the inference ($0.46 > 0.41$), which may be caused by numerical error accumulation induced by a very low value of q .

Fig. 9e gives the predicted relative activities during the 10th loading cycle for $q = 0.1$ and $q = 1.0$. It can be seen that for the two cases, prismatic slip increases with the decrease of tensile twinning during tension reversal from E_{12} to E_2 and it becomes more active near the tensile peak for $q = 0.1$ than for $q = 1.0$. Similar trends for relative activities can be found at each loading cycle which causes the unexpected strain hardening effect close to tensile peaks for $q = 0.1$ (Fig. 9a). In addition, during compression reversals for the two cases, prismatic slip is observed to be activated from the strain of $\sim x223C-1\%$ to -2% and rapidly increases with the rapid decrease of detwinning. Furthermore, for $q = 0.1$, pyramidal slip is found to be activated to contribute to plastic deformation at the very late stage of compression reversal, however, closer examination shows that the more active prismatic slip is still responsible for the stronger strain hardening effect at the late stage of compression reversal for $q = 0.1$ compared with the other two cases (Figs. 9a, b, and c). In general, it can be concluded that the smaller the parameter q is, the stronger the strain hardening effect at the late stage of tension and compression reversals would be. In addition, the cyclic plastic response for $q = 0.5$ seems much closer to that for $q = 1.0$ than for $q = 0.1$.

3.2.5. detwinning behavior

As is well known that detwinning plays a key role in deformation mechanisms of Mg alloys under cyclic loading. In this study, simulations show that detwinning occurs during each loading cycle of all material orientations with strain amplitudes of 2%, 3%, and 4%. For the 0° (RD) and 22.5° material orientations, detwinning is found to contribute to plastic deformation during each tension reversal. Detwinning is also observed to be activated for the 45° material orientation during each tension and compression loading reversals while detwinning only occurs during each compression reversal for the 90° (ND) material orientation. From Figs. 5d and e, it can be seen that for the 67.5° and 90° (ND) material orientations, the current model overestimates the measured stabilized stress-strain

hysteresis loop during compression reversal from strain of 2% to 0 which is closely related to detwinning. However, the real issue might be that the current model could not well predict the measured inelastic stress-strain response (pseudo-elasticity) for the 67.5° and 90° (ND) material orientations under cyclic loading and unloading.

Numerical and experimental studies have been conducted in literature on the pseudo-elasticity behavior during loading-unloading process and concluded that the inelastic stress-strain response during unloading arises from the activation of basal slip and/or detwinning depending on the initial texture and deformation history. The general consensus on this topic is that basal slip contributes to inelastic strain during unloading if twinning is not activated during the loading process (e.g., Hama et al., 2011; Lee et al., 2014), and the pseudo-elasticity behavior is mainly ascribed to detwinning if twinning dominates previous deformation before unloading (e.g., Cáceres et al., 2003; Mann et al., 2007; Muránsky et al., 2009; Hama et al., 2013). However, controversies do exist on when detwinning is activated upon the subsequent unloading process if twinning is a main contributor during the previous loading. Some concluded in their studies that detwinning occurs immediately upon unloading (Wu et al., 2008; Zhang et al., 2021b) or at the early stage of

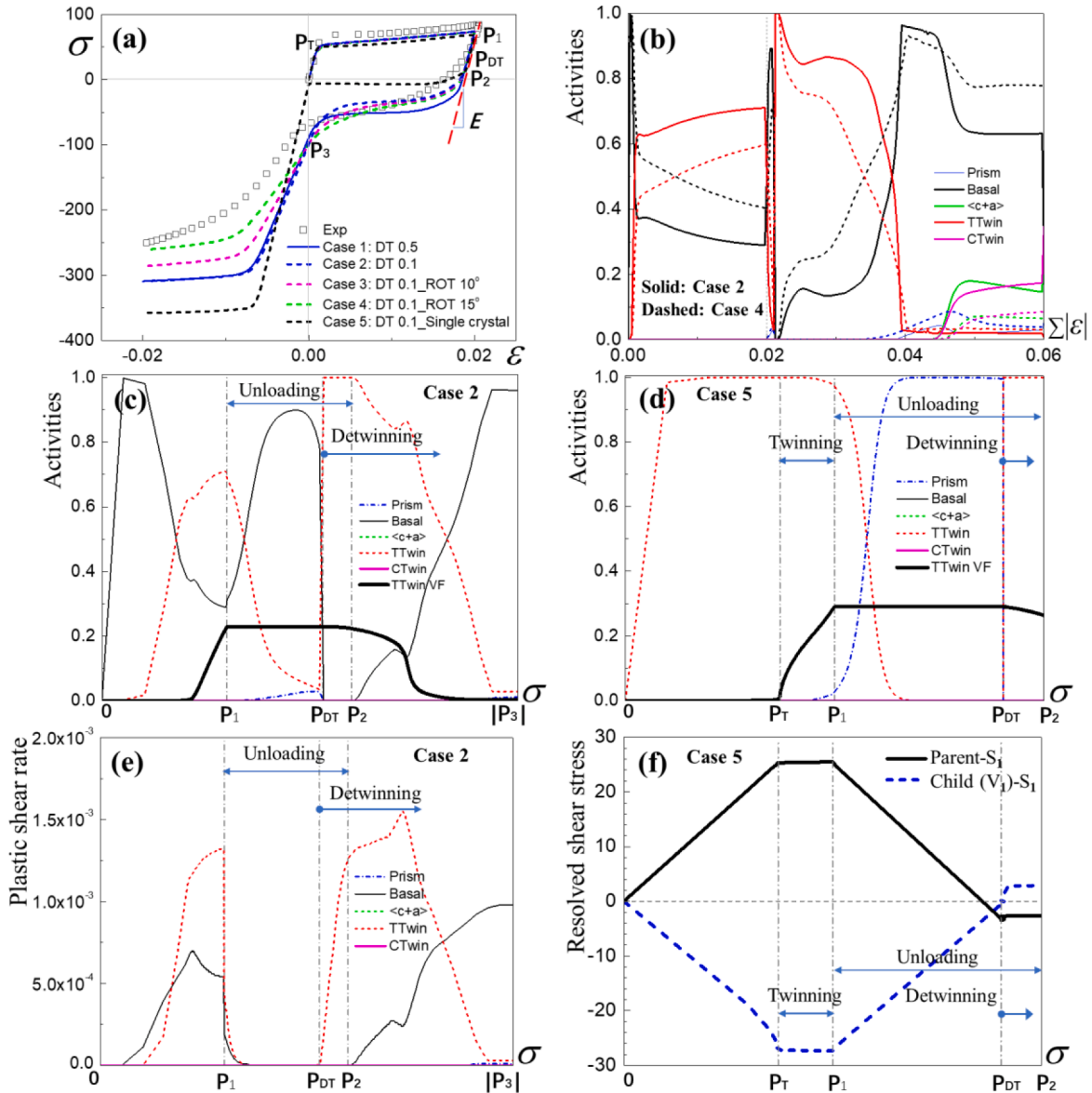


Fig. 10. Measured (symbols) and calculated (lines) stress-strain curves under tension and reverse compression to strain of 2% for the 90° (ND) material orientation with different cases (Cases 1–5) (a), and the predicted relative activities versus accumulated strain for Cases 2 and 4 (b). The relative activities (c) and plastic shear rate (e) versus stress for Case 2. The predicted relative activities (d), and the resolved shear stresses (f) on the plane of twin system S_1 of the single crystal and the twin variant (V_1) corresponding to the twin system S_1 for Case 5. P_T and P_{DT} respectively denote the stress values at the start of twinning and detwinning. P_1 , P_2 , and P_3 are the stress values at the tension peak, zero stress, the stress at strain of zero, respectively.

unloading (Lee and Gharghour, 2013), others found that detwinning is activated at the late stage of unloading process (Hama et al., 2013; Wang et al., 2013, 2020b), and still others observed that no apparent detwinning occurs during unloading (Uota et al., 2009; Wu et al., 2013, 2014). In this subsection, we will numerically explore the roles of detwinning and basal slip in contributing to inelastic stress-strain response for the 0° (ND) material orientation upon unloading after previous tensile loading.

Fig. 10 presents the measured and calculated stress-strain curves of the 0° (ND) material orientation under tension up to strain of 2% and reverse compression to -2%. In this figure, we give the calculated stress-strain curves for five cases. Case 1, referred to as 'DT 0.5', is the base case where the material parameters listed in Table 1 are used with the initial CRSS of detwinning is set to be half of that for twinning ($\tau_{0C}(\tau_{0D})=0.5\tau_{0A}(\tau_{0B})$). In Case 2, referred to as 'DT 0.1', we decrease the initial CRSS of detwinning to be $\tau_{0C}(\tau_{0D})=0.1\tau_{0A}(\tau_{0B})$. Based on Case 2, we consider three other cases with different textures: the initial texture rotated around the TD by 10° ('ROT 10°', see Case 3) or 15° ('ROT 15°', see Case 4) towards the RD and a single crystal with the orientation of (0°,0°,0°) (Case 5).

From Fig. 10a, it is seen that for the base case (Case 1), the current model could not capture the measured strong inelastic stress-strain response during unloading, and the calculated flow data exhibits no inelasticity until the very early stage of the reverse loading. It seems that detwinning could not be activated to contribute to inelastic deformation upon unloading, therefore, we decrease the initial CRSS of detwinning in Case 2. The calculated stress-strain curve shows a better agreement with experimental data than that in Case 1, however, the inelastic response is predicted to start only at the very end of the unloading process which can be confirmed by the fact that the plastic shear rate for all deformations modes is found to be almost zero from P_1 to P_{DT} and that for detwinning arises rapidly from P_{DT} to P_2 (See Fig. 10e), and the fact that the twin VF stays unchanged from P_1 to P_{DT} and slightly decrease from P_{DT} to P_2 although twinning is observed to be relatively dominant within this range (See Fig. 10c). The simulation results of Case 2 indicate that the material deforms almost elastically from P_1 to P_{DT} and detwinning occurs to accommodate inelastic deformation from P_{DT} to P_2 . In addition, since the initial texture of the ND material direction is a strong basal texture, we also consider a single crystal with the orientation of (0°,0°,0°) as a simplified problem (Case 5). In Case 5, for clarity, we discard the strain hardening effect for twinning and detwinning, so the CRSS for twinning and detwinning should be 27 MPa and 2.7 MPa, respectively. Figs. 10d and f present the resolved shear stress (RSS) on the plane of twin system S_1 of the single crystal and the twin variant (V_1) corresponding to the twin system S_1 . It is seen that the single crystal elastically deforms up to P_T and the RSS of the parent grain increases accordingly and reaches $\sim x223C27$ MPa at P_T . Twinning dominates plastic deformation during P_T to P_1 and the twin VF reaches $\sim x223C0.28$ at P_1 . During unloading process (P_1 to P_2), the single crystal elastically deforms up to the very end stage of unloading (P_{DT}) with twin VF being unchanged from P_1 to P_{DT} , and the RSS of the parent grain decreases within this range and becomes negative at P_{DT} while the RSS of its child (twin variant V_1) increases accordingly and becomes positive at P_{DT} . After that, detwinning starts to contribute to plastic deformation as the RSS of the child grain reaches $\sim x223C2.7$ MPa and so twin VF starts to decrease. In summary, for the single crystal with the orientation of (0°,0°,0°) under loading and unloading along the ND, the RSS of the child grain at the tensile peak (P_1) is negative and the single crystal elastically deforms during subsequent unloading until the RSS of the child grain reaches its initial CRSS, after that detwinning is activated to accommodate inelastic deformation. Therefore, the initial CRSS of detwinning along with the RSS of the twinned grain at the end of previous loading can determine whether and when the twinned grain can undergo detwinning to generate inelastic deformation during unloading. Based on comparisons of stress-strain responses between Case 2 and Case 5, it seems that the ND material orientation deforms similarly to the single crystal with the orientation of (0°,0°,0°) during the unloading process due to the initial strong basal texture. Therefore, it could be reasonable that inelastic behavior is only observed to start at the very end of unloading process even if the initial CRSS of detwinning is set to be one tenth of that for twinning.

As mentioned before, basal slip is another contributor for inelastic response of stress-strain curve during unloading. To increase the effect of basal on plastic response, we consider the other two cases (Cases 3 and 4). Fig. 10a shows that the predicted stress-strain curves during unloading process almost remain unchanged for Cases 2, 3, and 4, however, a better agreement with the measured data during the reversed compression from strain of $\sim x223C-0.5\%$ to -2.0% could be obtained for Cases 3 and 4 where basal is more active than that for Case 2 (Fig. 10b). Closer examination indicates that the plastic shear rate of basal slip during unloading process is almost zero (similar to Fig. 10e, not shown here) even for the texture rotated by 15° (Case 4). In addition, for Cases 2 and 4, the calculated weighted average values of the maximum Schmid Factor (SF) of all slip systems of each grain over the aggregate upon unloading at the tensile peak are respectively $\sim x223C0.243$ and $\sim x223C0.3$ which are not very favorable for the activation of basal slip. Furthermore, numerical tests show that decreasing the initial CRSS (τ_0^a) of basal slip will underestimate the initial macro-yielding of the 45° material orientation under monotonic tension and a lower back-extrapolated CRSS ($\tau_0^a + \tau_1^a$) for basal slip will cause underestimation of the measured monotonic tension flow curve at large strains. Therefore, it seems very hard to reproduce the measured inelastic response upon unloading by adjusting the material parameters for detwinning and basal slip based on the current EVPSC-TDT model and the initial texture.

It is worth noting that the initial texture used in the current model may also contribute to the observed discrepancies between the simulations and experimental data as it could possibly be collected from different patches of the same material or different locations of the bulk material and may not be the good representative of the real texture of the measured specimens (Qiao et al., 2015b), which deserves further attention.

3.3. Further discussion

3.3.1. Inelastic behavior and initial CRSS of detwinning

As mentioned above, Zhang et al. (2021b) investigated the onset of detwinning in a strongly basal-textured AZ31 alloy (grain size, 3 μm to 30 μm) under tension (or compression) up to strain of 7.5% (-7.5%) and subsequent compression (or tension) along the ND (or

RD) with real-time in situ synchrotron X-ray diffraction and observed that detwinning occurs immediately upon unloading, regardless of whether the twins were generated previously under tension along the ND or compression along the RD. In contrast, Wu et al. (2014) concluded that for a strongly basal textured AZ31B alloy (grain size, 40 μm), no apparent detwinning is experimentally observed during unloading subsequent to compression along the RD (up to strain of -7%) which was also confirmed by the numerical modeling based on the EVPSC-TDT model in their study. It is clear that the above two studies drew quite different conclusions on similar materials under similar pre-unloading deformation history. It is worth noting that Cáceres et al. (2003) pointed out that detwinning induced pseudoelastic effects could be enhanced by smaller grain size. In addition, Wang et al. (2020b) proposed that prismatic (a) or pyramidal (c + a) dislocations generated before unloading are effective to impede reversible movement of basal (a) dislocations and detwinning during unloading. In short, detwinning-induced inelastic behavior is closely related to sample microstructure, thermal treatment history (Zhang et al., 2021b), and deformation history. So the root causes of inelastic behavior are still not quite clear and deserve more experimental and numerical investigations.

From a mechanical point of view, Muránsky et al. (2009) pointed out that polycrystal grains which have experience twinning prior the peak stress of previous loading might in fact show quite high tensile stresses during loading at low applied compression stress, such internal tensile stress induced by redistribution of applied stress within the polycrystal upon unloading could cause detwinning during unloading. Therefore, we can consider that the magnitude of internal tensile stress upon unloading together with that of the activation stress for detwinning should govern when or whether detwinning will occur during unloading.

It is noted that from a macroscopic perspective, detwinning appears easier than twinning because there is no requirement for nucleation of detwinning (Qiao et al., 2015b), and twin nucleation does require a higher stress level (Partridge, 1965; Cui et al., 2017; Louca et al., 2021). Therefore, we set the initial CRSS for the four twinning operations A, B, C and D as $\tau_{0C}(\tau_{0D}) = 0.5\tau_{0A}(\tau_{0B})$ to approximately describe the apparent characteristics in the current model, which is different from what we did in our previous study (Qiao et al., 2015b) where discrimination of initial CRSS was made between twin nucleation and twin growth as $\tau_{0A} > \tau_{0B} = \tau_{0C} = \tau_{0D}$. Numerical results show that for the ND material orientation, setting a low value of initial CRSS of detwinning ($\tau_{0C}(\tau_{0D}) = 0.5(\tau_{0B})$) does give better prediction of the measured stress-strain curves during compression reversal, but the measured obvious inelastic response during unloading from tension peak to zero-stress point still could not be captured. It is admitted that a much lower initial CRSS of detwinning (e.g., $\tau_{0C}(\tau_{0D}) = 0.1(\tau_{0B})$) could further improve the prediction of stress-strain response during compression reversal from the zero-stress point to zero strain point, however, the measured inelastic behavior during unloading for the ND material orientation still could not be improved (see Case 2 in last subsection), and other simulation results would get worse (e.g., the upper branch of stabilized stress-strain hysteresis loop for the RD material orientation with 3% and 4% strain amplitude). Therefore, as a compromise we remain the initial CRSS of detwinning being half of that of twinning. The reason why the current model could not capture the measured strong inelastic behavior upon unloading could arise from the fact that the current mean field model based on self-consistent schemes might not properly describe some microstructure related properties of the Mg AZ31 plate and so underestimates the internal tensile stresses of twinned grains before unloading, which deserves further investigation.

3.3.2. Evolution of residual twinning and strain hardening of detwinning

It is noted that the lower branch of the measured stabilized stress-strain hysteresis loop of the 0° material orientation with 3% and 4% strain amplitudes could not be predicted well especially from the zero-strain point to the compression stress peak. The reason could be explained in terms of the following two aspects. First, in the current study, we assume the evolution of residual twins during cyclic loading follow the equation (Eq. (5)) proposed by Yu et al. (2014). Two parameters are introduced in this equation with f_{sat}^α denoting the saturated VF of residual twin and b_{tw}^α representing the material parameter governing the rate of saturation of residual twins. The parameter b_{tw}^α determines the number of loading cycles for residual twinning to be saturated at f_{sat}^α , and the two parameters might not have to be the same for different material orientations with different strain amplitudes. Furthermore, numerical results show that the two parameters (b_{tw}^α and f_{sat}^α) along with the parameter (q) governing fresh twinning actually interact with each other. Therefore, more experiments are desired to quantify these parameters and further verify the predictability of the employed equation in describing residual twinning. Second, very recently, Zhang et al. (2019) and Zhang et al. (2021a) employed two different sets of hardening parameters for twinning and detwinning in their simulations. It would be admitted that by doing so, improved predictions might be obtained for detwinning-associated flow curves. However, without strong evidence and for minimization of the number of material parameters, we choose to use the same hardening parameters for both twinning and detwinning (see, Table 1).

4. Conclusions

In the present paper, the EVPSC-TDT model has been employed to mimic the stabilized stress-strain hysteresis loops of the rolled AZ31B plate under cyclic loadings along five different material orientations and with three different strain amplitudes. For the total of 15 cases considered, we have very carefully examined numerical results for each cycle and compared them to the corresponding experimental data. It has been demonstrated that with the single set of the parameters, the EVPSC-TDT model with the improved empirical description of the residual twinning is able to capture the key features observed experimentally during the entire cyclic loading processes considered. In summary, the numerical results allow the following conclusions to be drawn:

- 1 The predicted stabilized stress-strain hysteresis loops for the 0° , 22.5° , 45° , 67.5° , and 90° material orientations are generally in good agreement with corresponding experimental data. The key features associated with twinning and detwinning are interpreted in terms of activities of deformation modes.

- 2 The Voce-type hardening law parameters in the EVPSC-TDT model are mainly determined by curve fitting of numerical results to monotonic experiments, however, in order to appropriately mimic the mechanical response under cyclic loadings, cyclic loading experiments should also be accounted for in determining these parameters. Specifically, to avoid unexpected cyclic hardening, the asymptotic hardening rate, h_1^a , of the extended Voce law for each deformation mode should be set to be zero, and cautious should be taken to employ large latent hardening coefficients in describing twin-slip and twin-twin interactions. It is also worth noting that the material parameters for basal slip are mainly obtained based on the measured data under monotonic tension/compression in the 45° material orientation.
- 3 The equation proposed by Yu et al. (2014) is employed to describe the evolution of residual twinning during cyclic loading, and a threshold equation with a new parameter, q , is proposed to constrain fresh twinning and retwinning. The saturated VF of residual twin f_{sat}^a and the parameter b_{tw}^a (see, Eq.(5)) governing the rate of saturation of residual twins as well as the parameter q in Eq. (9) are determined based on the measured stabilized stress-strain responses of the 45° and 90° (ND) material orientations. The effects of these parameters on cyclic plastic response have been investigated, and more experiments are desired to clearly quantify these parameters.
- 4 To approximately describe the apparent easier reverse movement of twin boundaries, the initial CRSSs for four twinning operations A, B, C and D are set as $\tau_{0C}(\tau_{0D})=0.5\tau_{0A}(\tau_{0B})$, while, for simplicity, the other voce-type hardening law parameters are kept the same for both twinning and detwinning. The effect of initial CRSS of detwinning on plastic response during reverse loading has been investigated.
- 5 The inelastic stress-strain response of the 90° (ND) material orientation during reverse loading has been numerically investigated. The inelastic behavior is predicted to occur at the very end of the unloading process for the 90° (ND) material orientation, which is ascribed to detwinning. It is assumed that the magnitude of internal tensile stress upon unloading together with that of the activation stress for detwinning should determine when or whether detwinning will occur during unloading. The discrepancies between numerical simulations and experimental data of the pseudo-elasticity behavior might be because the current mean field model based on self-consistent schemes might not properly describe some microstructure related properties of the Mg AZ31B plate and so underestimates the internal tensile stresses of twinned grains before unloading, which deserves further investigation.
- 6 Note that experimental validation of the calculated relative activities for various deformation modes is lack in the current study as the direct validation of the predicted relative activities is experimentally very hard, however, the deformation mechanisms obtained from the current model might be validated by comparisons with intensity changes and internal strain evolutions observed using *in-situ* neutron diffraction, which deserves further study in future work.
- 7 Tensile twinning and detwinning are closely related to fatigue damage and fracture of Mg alloys under cyclic loading with relatively large strain amplitudes. Numerical and experimental studies of the residual twinning, fresh twinning and retwinning behavior under cyclic loading are important for better understanding of the mechanisms of accumulation of fatigue damage and final failure in Mg alloys, which should be valuable in developing reasonable fatigue damage and fracture models and can potentially facilitate manipulation of the microstructure and mechanical properties of Mg alloys for further structural applications.

Authorship contributions

F.H. Wang: Visualization, Formal analysis, Data Curation, Investigation, Validation, Writing-Review & Editing

H. Qiao: Formal analysis, Writing-original draft, Writing-Review & Editing, Validation

Y.Q. Wang: Data Curation, Resources

J. Dong: Supervision, Validation

Y.Y. Jiang: Supervision, Data Curation, Resources

P.D. Wu: Visualization, Supervision, Validation, Writing-Review & Editing

This statement is signed by the corresponding author on behalf of all the other authors.

Declaration of Competing Interest

The authors declare that they have no known competing financial interests or personal relationships that could have appeared to influence the work reported in this paper.

Acknowledgments

P.D. Wu was supported by the Natural Sciences and Engineering Research Council of Canada (NSERC, project No: RGPIN-2016-06464). F.H. Wang and J. Dong were supported by the National Natural Science Foundation of China (Nos. 52071211, 52071208).

References

- Anes, V., Reis, L., Freitas, M., 2019. Evaluation of a phenomenological elastic-plastic approach for magnesium alloys under multiaxial loading conditions. *Fatigue Fract. Eng. Mater. Struct.* 42, 2468–2486.
- Anten, K., Scholtes, B., 2019. Formation of macroscopic twin bands and inhomogeneous deformation during cyclic tension-compression loading of the Mg-wrought alloy AZ31. *Mater. Sci. Eng. A* 746, 217–228.
- Asaro, R.J., Needleman, A., 1985. Texture development and strain hardening in rate dependent polycrystals. *Acta. metall.* 33, 923–953.

- Bettles, C.J., Gibson, M.A., 2005. Current wrought magnesium alloys: strengths and weaknesses. *JOM* 57, 46–49.
- Bhattacharyya, J.J., Kada, S.R., Barnett, M.R., Agnew, S.R., 2019. Crystal plasticity and in-situ diffraction-based determination of the dislocation strengthening and load-sharing effects of precipitates in Mg alloy. *AZ91. Mater.* 6, 100308.
- Bong, H.J., Lee, J., Hu, X., Sun, X., Lee, M.G., 2020. Predicting forming limit diagrams for magnesium alloys using crystal plasticity finite elements. *Int. J. Plast.* 126, 102630.
- Briffod, F., Shiraiwa, T., Enoki, M., 2019. Numerical investigation of the influence of twinning/detwinning on fatigue crack initiation in AZ31 magnesium alloy. *Mater. Sci. Eng. A* 753, 79–90.
- Cáceres, C.H., Sumitomo, T., Veidt, M., 2003. Pseudoelastic behaviour of cast magnesium AZ91 alloy under cyclic loading-unloading. *Acta. Mater.* 51, 6211–6218.
- Castro, F., Jiang, Y., 2017. Fatigue of extruded AZ31B magnesium alloy under stress- and strain-controlled conditions including step loading. *Mech. Mater.* 108, 77–86.
- Chapuis, A., Liu, Q., 2018. Effect of strain rate sensitivity in visco-plastic modeling. *Int. J. Solids. Struct.* 152–153, 217–227.
- Chen, G., Lu, L., Cui, Y., Xing, R., Gao, H., Chen, X., 2015. Ratcheting and low-cycle fatigue characterizations of extruded AZ31B Mg alloy with and without corrosive environment. *Int. J. Fatigue.* 80, 364–371.
- Chen, G., Ren, J., Gao, H., Cui, Y., Chen, X., 2017. Pseudoelastic and corrosion behaviors of Mg ZEK100 alloy under cyclic loading. *Int. J. Fatigue.* 103, 466–477.
- Cui, Y., Li, Y., Wang, Z., Ding, X., Koizumi, Y., Bian, H., Lin, L., Chiba, A., 2017. Impact of solute elements on detwinning in magnesium and its alloys. *Int. J. Plast.* 91, 134–159.
- Denk, J., Nischler, A., Whitmore, L., Huber, O., Saage, H., 2019. Discontinuous and inhomogeneous strain distributions under monotonic and cyclic loading in textured wrought magnesium alloys. *Mater. Sci. Eng. A* 764, 138182.
- Dong, S., Yu, Q., Jiang, Y., Dong, J., Wang, F., Ding, W., 2015. Electron backscatter diffraction observations of twinning-detwinning evolution in a magnesium alloy subjected to large strain amplitude cyclic loading. *Mater. Des.* 65, 762–765.
- Fallahi, H., Mohammad, T., Chris Davies, C., 2020. Evolution of anelastic behaviour and twinning in cyclic loading of extruded magnesium alloy ZM21. *Mater. Sci. Eng. A* 770, 138520.
- Feather, W.G., Savage, D.J., Knezevic, M., 2021. A crystal plasticity finite element model embedding strain-rate sensitivities inherent to deformation mechanisms: application to alloy AZ31. *Int. J. Plast.* 143, 103031.
- Feng, B., Bronkhorst, C.A., Liu, Z., Morrow, B.M., Cerreta, E.K., Li, W.H., Daphalapurkar, N.P., 2020. Three-dimensional modeling and simulations of single-crystal and bi-crystal titanium for high-strain-rate loading conditions. *Int. J. Plast.* 133, 102771.
- Frydrych, K., Libura, T., Kowalewski, Z., Maj, M., Kowalczyk-Gajewska, K., 2021. On the role of slip, twinning and detwinning in magnesium alloy AZ31B sheet. *Mater. Sci. Eng. A* 813, 141152.
- Ganesan, S., Yaghoobi, M., Githens, A., Chen, Z., Daly, S., Allison, J.E., Sundararaghavan, V., 2021. The effects of heat treatment on the response of WE43 Mg alloy: crystal plasticity finite element simulation and SEM-DIC experiment. *Int. J. Plast.* 137, 102917.
- Gu, C.F., Tóth, L.S., 2012. Polycrystal modeling of tensile twinning in a Mg alloy during cyclic loading. *Scr. Mater.* 67, 673–676.
- Gu, C.F., Tóth, L.S., Hoffman, M., 2014. Twinning effects in a polycrystalline magnesium alloy under cyclic deformation. *Acta Mater* 62, 212–224.
- Guo, X.Q., Chapuris, A., Wu, P.D., Agnew, S.R., 2015. On twinning and anisotropy in rolled Mg alloy AZ31 under uniaxial compression. *Int. J. Solids. Struct.* 64–65, 42–50.
- Guo, X., Ma, C., Zhao, L., Chapuis, A., Liu, Q., Wu, P., 2021. Effect of pre-deformation on the activation stress of {10-12} twinning in Mg-3Al-1Zn alloy. *Mater. Sci. Eng. A* 800, 140384.
- Habib, S.A., Lloyd, J.T., Meredith, C.S., Khan, A.S., Schoenfeld, S.E., 2019. Predicting textural variability effects in the anisotropic plasticity and stability of hexagonal metals: application to magnesium and its alloys. *Int. J. Plast.* 122, 285–318.
- Hama, T., Takuda, H., 2011. Crystal-plasticity finite-element analysis of inelastic behavior during unloading in a magnesium alloy sheet. *Int. J. Plast.* 27, 1072–1092.
- Hama, T., Kariyazaki, Y., Hosokawa, N., Fujimoto, H., Takuda, H., 2012. Work-hardening behaviors of magnesium alloy sheet during in-plane cyclic loading. *Mater. Sci. Eng. A* 551, 209–217.
- Hama, T., Kitamura, N., Takuda, H., 2013. Effect of twinning and detwinning on inelastic behavior during unloading in a magnesium alloy sheet. *Mater. Sci. Eng. A* 583, 232–241.
- Hama, T., Suzuki, T., Hatakeyama, S., Fujimoto, H., Takuda, H., 2018. Role of twinning on the stress and strain behaviors during reverse loading in rolled magnesium alloy sheets. *Mater. Sci. Eng. A* 725, 8–18.
- Han, F., Rosters, F., Raabe, D., 2020. Microstructure-based multiscale modeling of large strain plastic deformation by coupling a full-field crystal plasticity-spectral solver with an implicit finite element solver. *Int. J. Plast.* 125, 97–117.
- Hu, X., Ji, Y., Chen, L., Lebensohn, R.A., Chen, L.Q., Cui, X., 2021. Spectral phase-field model of deformation twinning and plastic deformation. *Int. J. Plast.* 143, 103019.
- Indurkar, P.P., Baweja, S., Perez, R., Joshi, S.P., 2020. Predicting textural variability effects in the anisotropic plasticity and stability of hexagonal metals: application to magnesium and its alloys. *Int. J. Plast.* 132, 102762.
- Jalili, M., Soltani, B., Papazafeiropoulos, G., Vu, Q.V., 2020. Micromechanical modeling of cyclic plastic deformation of ZK60 Mg alloy using 3D full-field crystal plasticity coupled with computational homogenization. *Int. J. Fatigue* 140, 105794.
- Kang, G., Yu, C., Liu, Y., Quan, G., 2014. Uniaxial ratcheting of extruded AZ31 magnesium alloy: effect of mean stress. *Mater. Sci. Eng. A* 607, 318–327.
- Kim, J.H., Kim, D., Lee, Y.S., Lee, M.G., Chung, K., Kim, H.Y., Wagoner, R.H., 2013. A temperature-dependent elasto-plastic constitutive model for magnesium alloy AZ31 sheets. *Int. J. Plast.* 50, 66–93.
- Knezevic, M., McCabe, R.J., Tomé, C.N., Lebensohn, R.A., Chen, S.R., Cady, C.M., Gray III, G.T., Mihaila, B., 2013. Modeling mechanical response and texture evolution of α -uranium as a function of strain rate and temperature using polycrystal plasticity. *Int. J. Plast.* 43, 70–84.
- Knezevic, M., Zecevic, M., Beyerlein, I.J., Lebensohn, R.A., 2016. A numerical procedure enabling accurate descriptions of strain rate-sensitive flow of polycrystals within crystal visco-plasticity theory. *Comput. Methods Appl. Mech. Eng.* 308, 468–482.
- Kok, S., Beaudoin, A.J., Tortorelli, D.A., 2002. A polycrystal plasticity model based on the mechanical threshold. *Int. J. Plast.* 18, 715–741.
- Lee, M.G., Wagoner, R.H., Lee, J.K., Chung, K., Kim, H.Y., 2008. Constitutive modeling for anisotropic/asymmetric hardening behavior of magnesium alloy sheets. *Int. J. Plast.* 24, 545–582.
- Lee, S.Y., Gharghoury, M.A., 2013. Pseudoelastic behavior of magnesium alloy during twinning-dominated cyclic deformation. *Mater. Sci. Eng. A* 572, 98–102.
- Lee, S.Y., Wang, H., Gharghoury, M.A., Nayeri, G., Woo, W., Shin, E., Wu, P.D., Poole, W.J., Wu, W., An, K., 2014. Deformation behavior of solid-solution-strengthened Mg-9wt.% Al alloy: in situ neutron diffraction and elastic-viscoplastic self-consistent modeling. *Acta. Mater.* 73, 139–148.
- Lee, J., Bong, H.J., Kim, S.J., Lee, M.G., Kim, D., 2020. An enhanced distortional-hardening-based constitutive model for hexagonal close-packed metals: application to AZ31B magnesium alloy sheets at elevated temperatures. *Int. J. Plast.* 126, 102618.
- Lei, Y., Li, H., Liu, Y., Wang, Z., Kang, G., 2021. Experimental study on uniaxial ratcheting-fatigue interaction of extruded AZ31 magnesium alloy with different plastic deformation mechanisms. *J. Magnes. Alloy.* <https://doi.org/10.1016/j.jma.2021.03.018>.
- Lftikhar, A., Khan, A.S., 2021. The Evolution of Yield Loci with Finite Plastic Deformation along Proportional & Non-proportional Loading Paths in an Annealed Extruded AZ31 Magnesium Alloy. *Int. J. Plast.* 143, 103007.
- Li, F.F., Fang, G., 2020a. Modeling of 3D plastic anisotropy and asymmetry of extruded magnesium alloy and its applications in three-point bending. *Int. J. Plast.* 130, 102704.
- Li, M., Lou, X.Y., Kim, J.H., Wagoner, R.H., 2010. An efficient constitutive model for room-temperature, low-rate plasticity of annealed Mg AZ31B sheet. *Int. J. Plast.* 26, 820–858.
- Li, Z., Zhou, G., Li, D., Jain, M.K., Peng, Y., Wu, P.D., 2020. Forming limits of magnesium alloy AZ31B sheet at elevated temperatures. *Int. J. Plast.* 135, 102822.
- Liao, X., Wang, J., Nie, J., Jiang, Y., Wu, P., 2016. Deformation twinning in hexagonal materials. *MRS Bulletin* 41, 314–319.
- Lin, T.H., 1957. Analysis of elastic and plastic strains of a face-centered cubic crystal. *J. Mech. Phys. Solids.* 5, 143–149.

- Lin, Y.C., Chen, X.M., Chen, G., 2011. Uniaxial ratcheting and low-cycle fatigue failure behaviors of AZ91D magnesium alloy under cyclic tension deformation. *J. Alloys Compd.* 509, 6838–6843.
- Ling, Y., Roostaie, A.A., Glinka, G., Jahed, H., 2019. Fatigue of ZEK100-F magnesium alloy: characterisation and modelling. *Int. J. Fatigue* 125, 179–186.
- Louca, K., Abdolvand, H., Mareau, C., Majkut, M., Wright, J., 2021. Formation and annihilation of stressed deformation twins in magnesium. *Commun. Mater.* 2 (9), 1–11.
- Ma, C., Wang, H., Hama, T., Guo, X., Mao, X., Wang, J., Wu, P., 2019. Twinning and detwinning behaviors of commercially pure titanium sheets. *Int. J. Plast.* 121, 261–279.
- Mann, G.E., Sumitomo I, T., Cáceres, C.H., Griffiths, J.R., 2007. Reversible plastic strain during cyclic loading-unloading of Mg and Mg-Zn alloys. *Mater. Sci. Eng. A* 456, 138–146.
- Maldar, A., Wang, L., Zhu, G., Zeng, X., 2020. Investigation of the alloying effect on deformation behavior in Mg by Visco-Plastic Self-Consistent modeling. *J. Magnes. Alloy.* 8, 210–218.
- Morrow, B.M., McCabe, R.J., Cerreta, E.K., Tomé, C.N., 2014. *In-situ TEM observation of twinning and detwinning during cyclic loading in Mg*. *Metall. Mater. Trans. A* 45, 36–40.
- Muhammad, W., Mohammadi, M., Kang, J., Mishra, R.K., Inal, K., 2015. An elasto-plastic constitutive model for evolving asymmetric/anisotropic hardening behavior of AZ31B and ZEK100 magnesium alloy sheets considering monotonic and reverse loading paths. *Int. J. Plast.* 70, 30–59.
- Muránsky, O., Carr, D.G., Sittner, P., Oliver, E.C., 2009. In situ neutron diffraction investigation of deformation twinning and pseudoelastic-like behaviour of extruded AZ31 magnesium alloy. *Int. J. Plast.* 25, 1107–1127.
- Murphy-Leonard, A.D., Pagan, D.C., Beaudoin, A., Miller, M.P., Allison, J.E., 2019. Quantification of cyclic twinning-detwinning behavior during low-cycle fatigue of pure magnesium using high energy X-ray diffraction. *Int. J. Fatigue* 125, 314–323.
- Nagra, J.S., Brahme, A., Lévesque, J., Mishra, R., Lebensohn, R.A., Inal, K., 2020. A new micromechanics based full field numerical framework to simulate the effects of dynamic recrystallization on the formability of HCP metals. *Int. J. Plast.* 125, 210–234.
- Nakata, T., Bhattacharyya, J.J., Agnew, S.R., Kamado, S., 2019. Unexpected influence of prismatic plate-shaped precipitates on strengths and yield anisotropy in an extruded Mg-0.3Ca-1.0In-0.1Al-0.2Mn (at.%) alloy. *Scr. Mater.* 169, 70–75.
- Nascimento, L., Yi, S., Bohlen, J., Fuskova, L., Letzig, D., Kainer, K.U., 2010. High cycle fatigue behaviour of magnesium alloys. *Procedia Eng.* 2, 743–750.
- Nguyen, N.T., Lee, M.G., Kim, J.H., Kim, H.Y., 2013. A practical constitutive model for AZ31B Mg alloy sheets with unusual stress-strain response. *Finite Elem. Anal. Des.* 76, 39–49.
- Nový, F., Janeček, M., Škorfk, V., Müller, J., Wagner, L., 2009. Very high cycle fatigue behaviour of as-extruded AZ31, AZ80, and ZK60 magnesium alloys. *Int. J. Mat. Res.* 100, 288–291.
- Paramatmuni, C., Zheng, Z., Rainforth, W.M., Dunne, F.P.E., 2020. Twin nucleation and variant selection in Mg alloys: an integrated crystal plasticity modelling and experimental approach. *Int. J. Plast.* 135, 102778.
- Paramatmuni, C., Guo, Y., Withers, P.J., Dunne, F.P.E., 2021. A three-dimensional mechanistic study of the drivers of classical twin nucleation and variant selection in Mg alloys: a mesoscale modelling and experimental study. *Int. J. Plast.* 143, 103027.
- Park, S.H., Hong, S.G., Bang, W., Lee, C.S., 2010. Effect of anisotropy on the low-cycle fatigue behavior of rolled AZ31magnesium alloy. *Mater. Sci. Eng. A* 527, 417–423.
- Partridge, P.G., 1965. Cyclic twinning in fatigued close-packed hexagonal metals. *Philos. Mag.* 12, 1043–1054.
- Qiao, H., Wu, P.D., Gharghour, M.A., Daymond, M.R., 2015a. Evaluation of elastic-viscoplastic self-consistent polycrystal plasticity models for zirconium alloys. *Int. J. Solids. Struct.* 71, 308–322.
- Qiao, H., Agnew, S.R., Wu, P.D., 2015b. Modeling twinning and de-twinning behavior of Mg alloy ZK60A during monotonic and cyclic loading. *Int. J. Plast.* 65, 61–84.
- Qiao, H., Xin, Y.C., Zong, Z.L., Wu, P.D., 2021. Effect of twinning on the yield surface shape of Mg alloy plates under in-plane biaxial loading. *Int. J. Solids. Struct.* 216, 211–221.
- Roostaie, A.A., Jahed, H., 2016. Role of loading direction on cyclic behaviour characteristics of AM30 extrusion and its fatigue damage modelling. *Mater. Sci. Eng. A* 670, 26–40.
- Roostaie, A.A., Jahed, H., 2018. A cyclic small-strain plasticity model for wrought Mg alloys under multiaxial loading: numerical implementation and validation. *Int. J. Mech. Sci.* 145, 318–329.
- You, S., Huang, Y., Kainer, K.U., Hort, N., 2017. Recent research and developments on wrought magnesium alloys. *J. Magnes. Alloy.* 5, 239–253.
- Sahoo, S.K., Biswas, S., Toth, L.S., Gautam, P.C., Beausir, B., 2020. Strain hardening, twinning and texture evolution in magnesium alloy using the all twin variant polycrystal modelling approach. *Int. J. Plast.* 128, 102660.
- Shafaghi, N., Kapan, E., Aydiner, C.C., 2020. Cyclic strain heterogeneity and damage formation in rolled magnesium via in situ microscopic image correlation. *Exp. Mech.* 60, 735–751.
- Singh, J., Kim, M.S., Kaushik, L., Kang, J.H., Kim, D., Martin, E., Choi, S.H., 2020. Twinning-detwinning behavior of E-form Mg alloy sheets during in-plane reverse loading. *Int. J. Plast.* 127, 102637.
- Slutsky, L.J., Garland, C.W., 1957. Elastic constants of magnesium from 4.2K to 300K. *Phys. Rev.* 107, 972–976.
- Tang, J., Fan, H., Wei, D., Jiang, W., Wang, Q., Tian, X., Zhang, X., 2020. Interaction between a {10-12} twin boundary and grain boundaries in magnesium. *Int. J. Plast.* 126, 102613.
- Tomé, C.N., Canova, G.R., Kocks, U.F., Christodoulou, N., Jonas, J.J., 1984. The relation between macroscopic and microscopic strain-hardening in FCC polycrystals. *Acta Metall.* 32, 1637–1653.
- Tomé, C.N., Lebensohn, R.A., Kocks, U.F., 1991. A model for texture development dominated by deformation twinning-application to zirconium alloys. *Acta Metall. Mater.* 39, 2667–2680.
- Tóth, L.S., Molinari, A., Zouhal, N., 2000. Cyclic plasticity phenomena as predicted by polycrystal plasticity. *Mech. Mater.* 32, 99–113.
- Uota, T., Suzu, T., Fukumoto, S., Yamamoto, A., 2009. EBSD observation for reversible behavior of deformation twins in AZ31B magnesium alloy. *Mater. Trans. A* 50, 2118–2120.
- Wang, F., Liu, M., Sun, J., Feng, M., Jin, L., Dong, J., Jiang, Y., 2019. Effects of initial {10-12} twins on cyclic deformation and fatigue of magnesium alloy at low strain amplitudes. *Mater. Charact.* 149, 118–123.
- Wang, F., Feng, M., Jiang, Y., Dong, J., Zhang, Z., 2020a. Cyclic shear deformation and fatigue of extruded Mg-Gd-Y magnesium alloy. *J. Mater. Sci. Technol.* 39, 74–81.
- Wang, H., Raesinia, B., Wu, P.D., Agnew, S.R., Tomé, C.N., 2010a. Evaluation of self-consistent crystal plasticity models for magnesium alloy AZ31B sheet. *Int. J. Solids. Struct.* 47, 2905–2917.
- Wang, H., Lee, S.Y., Wang, H., Woo, W., Huang, E.W., Jain, J., An, K., 2020b. On plastic anisotropy and deformation history-driven anelasticity of an extruded magnesium alloy. *Scr. Mater.* 176, 36–41.
- Wang, H., Lee, S.Y., Huang, E.W., Jain, J., Li, D., Peng, Y., Choi, H.S., Wu, P., 2020f. Crystal plasticity modeling and neutron diffraction measurements of a magnesium AZ31B plate: effects of plastic anisotropy and surrounding grains. *J. Mech. Phys. Solids.* 135, 103795.
- Wang, H., Wu, P.D., Tomé, C.N., Huang, Y., 2010b. A finite strain elastic-viscoplastic self-consistent model for polycrystalline materials. *J. Mech. Phys. Solids.* 58, 594–612.
- Wang, H., Wu, P.D., Tomé, C.N., Wang, J., 2012. A constitutive model of twinning and detwinning for hexagonal close packed polycrystals. *Mater. Sci. Eng. A* 555, 93–98.
- Wang, H., Wu, P.D., Wang, J., Tomé, C.N., 2013a. A physics-based crystal plasticity model for hexagonal close packed (HCP) crystals including both twinning and detwinning mechanisms. *Int. J. Plast.* 49, 2155–2167.
- Wang, H., Wu, P.D., Wang, J., 2013b. Modeling inelastic behavior of magnesium alloys during cyclic loading-unloading. *Int. J. Plast.* 47, 49–64.
- Wang, H., Wu, P.D., Wang, J., 2015. Modelling the role of slips and twins in magnesium alloys under cyclic shear. *Comput. Mater. Sci.* 96, 214–218.

- Wang, H., Wu, P.D., Kurukuri, S., Worswick, M.J., Peng, Y., Tang, Ding, Li, D., 2018. Strain rate sensitivities of deformation mechanisms in magnesium alloys. *Int. J. Plast.* 107, 207–222.
- Wang, J., Zecevic, M., Knezevic, M., Beyerlein, I.J., 2020. Polycrystal plasticity modeling for load reversals in commercially pure titanium. *Int. J. Plast.* 125, 294–313.
- Wang, J., Ferdowsi, M.R.G., Kada, S.R., Lynch, P.A., Wang, Z., Kimpton, J.A., Barnett, M.R., 2021. Stress relaxations during cyclic loading-unloading in precipitation hardened Mg-4. *Acta Mater* 205, 116531.
- Wang, Q., Cochrane, C., Skippon, T., Wang, Z., Abdolvand, H., Daymond, M.R., 2020d. Orientation-dependent irradiation hardening in pure Zr studied by nanoindentation, electron microscopies, and crystal plasticity finite element modeling. *Int. J. Plast.* 124, 133–154.
- Wang, Y., Culbertson, D., Jiang, Y., 2020e. An experimental study of anisotropic fatigue behavior of rolled AZ31B magnesium alloy. *Mater. Des.* 186, 108266.
- Wu, B., Song, L., Duan, G., Du, X., Wang, Y., Esling, C., Philippe, M.J., 2020. Effect of cyclic frequency on uniaxial ratcheting behavior of a textured AZ31B magnesium alloy under stress control. *Mater. Sci. Eng. A* 795, 139675.
- Wu, L., Jain, A., Brown, D.W., Stoica, G.M., Agnew, S.R., Clausen, B., Fielden, D.E., Liaw, P.K., 2008. Twinning-detwinning behavior during the strain-controlled low-cycle fatigue testing of a wrought magnesium alloy, ZK60A. *Acta Mater.* 56, 688–695.
- Wu, P.D., Guo, X.Q., Qiao, H., Agnew, S.R., Lloyd, D.J., Embury, J.D., 2017. On the rapid hardening and exhaustion of twinning in magnesium alloy. *Acta Mater.* 122, 369–377.
- Wu, P.D., Neale, K.W., Van der Giessen, E., 1996. Simulation of the behaviour of FCC polycrystals during reversed torsion. *Int. J. Plast.* 12, 1199–1219.
- Wu, W., An, K., Huang, L., Lee, S.Y., Liaw, P.K., 2013. Deformation dynamics study of a wrought magnesium alloy by real-time in situ neutron diffraction. *Scr. Mater.* 69, 358–361.
- Wu, W., Qiao, H., An, K., Guo, X.Q., Wu, P.D., Liaw, P.K., 2014. Investigation of deformation dynamics in a wrought magnesium alloy. *Int. J. Plast.* 62, 105–120.
- Xie, D., Lyu, Z., Li, Y., Liaw, P.K., Chew, H.B., Ren, Y., Chen, Y., An, K., Gao, Y., 2021. In situ monitoring of dislocation, twinning, and detwinning modes in an extruded magnesium alloy under cyclic loading conditions. *Mater. Sci. Eng. A* 806, 140860.
- Xiong, Y., Yu, Q., Jiang, Y., 2012. Multiaxial fatigue of extruded AZ31B magnesium alloy. *Mater. Sci. Eng. A* 546, 119–128.
- Xing, Z., Fan, H., Tang, J., Wang, B., Kang, G., 2021. Molecular dynamics simulation on the cyclic deformation of magnesium single crystals. *Comput. Mater. Sci.* 186, 110003.
- Yaghoobi, M., Allison, J.E., Sundararaghavan, V., 2020. Multiscale modeling of twinning and detwinning behavior of HCP polycrystals. *Int. J. Plast.* 127, 102653.
- Yu, C., Kang, G., Kan, Q., 2014. Crystal plasticity based constitutive model for uniaxial ratcheting of polycrystalline magnesium alloy. *Comput. Mater. Sci.* 84, 63–73.
- Yu, Q., Zhang, J., Jiang, Y., 2011. Direct observation of twinning-detwinning-retwinning on magnesium single crystal subjected to strain-controlled cyclic tension-compression in [0001] direction. *Philos. Mag. Lett.* 91, 757–765.
- Yu, Q., Zhang, J., Jiang, Y., Li, Q., 2012. An experimental study on cyclic deformation and fatigue of extruded ZK60 magnesium alloy. *Int. J. Fatigue* 36, 47–58.
- Zecevic, M., Knezevic, M., McWilliams, B., Lebensohn, R.A., 2020. Modeling of the thermo-mechanical response and texture evolution of WE43 Mg alloy in the dynamic recrystallization regime using a viscoplastic self-consistent formulation. *Int. J. Plast.* 130, 102705.
- Zhao, L., Guo, X.Q., Chapuis, A., Xin, Y.C., Liu, Q., Wu, P.D., 2019. Strain-path dependence of {10-12} twinning in a rolled Mg-3Al-1Zn alloy: influence of twinning model. *Metall. Mater. Trans. A* 50A, 118–131.
- Zhou, A.G., Basu, S., Barsoum, M.W., 2008. Kinking nonlinear elasticity, damping and microyielding of hexagonal close-packed metals. *Acta Mater* 56, 60–67.
- Zouhal, N., Molinari, A., Toth, L.S., 1996. Elastic-plastic effects during cyclic loading as predicted by the Taylor-Lin model of polycrystal elasto-viscoplasticity. *Int J Plast* 12, 343–360.
- Zhang, X.P., Castagne, S., Luo, X.F., Gu, C.F., 2011. Effects of extrusion ratio on the ratcheting behavior of extruded AZ31B magnesium alloy under asymmetrical uniaxial cyclic loading. *Mater. Sci. Eng. A* 528, 838–845.
- Zhang, H., Jérusalem, A., Salvati, E., Papadaki, C., Fong, K.S., Song, X., Korsunsky, A.M., 2019. Multi-scale mechanisms of twinning-detwinning in magnesium alloy AZ31B simulated by crystal plasticity modeling and validated via in situ synchrotron XRD and in situ SEM-EBSD. *Int. J. Plast.* 119, 43–56.
- Zhang, M., Zhang, H., Ma, A., Llorca, J., 2021a. Experimental and numerical analysis of cyclic deformation and fatigue behavior of a Mg-RE alloy. *Int. J. Plast.* 139, 102885.
- Zhang, N.B., Zhang, Y.Y., Chen, S., Zhang, B.B., Li, Z.L., Xie, H.L., Lu, L., Yao, X.H., Luo, S.N., 2021b. Onset of detwinning in Mg-3Al-1Zn alloy: a synchrotron-based X-ray diffraction study. *Scr. Mater.* 190, 113–117.
- Zhu, G., Wang, L., Sun, Y., Shang, X., Wang, J., Wang, H., Zeng, X., 2021. Grain-size effect on the deformation of Mg-3Al-3Sn alloy: experiments and elastic-viscoplastic self-consistent modeling. *Int. J. Plast.* 143, 103018.